Capsaicin acts as a novel NRF2 agonist to suppress ethanol induced gastric mucosa oxidative damage by directly disrupting the KEAP1-NRF2 interaction

Xiaoning Gao[1, †], Bo Zhang[2, 3, †], Peiyuan Liu[1, †], Mingyue Yuwen[1], Zixiang Liu[1], Ruyang Tan[1], Boyang Wang[3], Kairui Liu[1], Zhiru Yang[1], Junli Ba[1], Xue Bai[1], Shiti Shama [1], Cong Tang[1], Liren Liu[2], Cheng Zhu[1, *], Tao Wang[1, *], Shao Li[3, *], Jun Kang[1, *]

[1] School of Life Sciences, Tianjin University, 92 Weijin Road, Nankai District, Tianjin 300072, People's Republic of China.

[2] Department of Molecular Pharmacology, Tianjin Medical University Cancer Institute & Hospital; National Clinical Research Center for Cancer; Key Laboratory of Cancer Prevention and Therapy, Tianjin; Tianjin's Clinical Research Center for Cancer, Tianjin 300060, China.

[3] Institute for TCM-X, MOE Key Laboratory of Bioinformatics, Bioinformatics Division, BNRist, Department of Automation, Tsinghua University, No. 30 Shuangqing Road, Haidian District, Beijing 100084, People's Republic of China.

* Correspondence:

Jun Kang, jun.kang@tju.edu.cn; Shao Li, shaoli@mail.tsinghua.edu.cn ;

Tao Wang, wangtaobio@tju.edu.cn; Cheng Zhu, cheng_zhu@tju.edu.cn

[†] These authors contributed equally to this work.

Abstract

Ethanol induced oxidative damage to the gastric mucosa is one of the causes of gastritis and gastric ulcers. The KEAP1/NRF2 system stands as the principal regulator of reactive oxygen stress (ROS). Capsaicin (CAP), a naturally small molecule from chili, is recognized for its antioxidant and anti-inflammatory attributes. Yet, the mechanistic action remains largely unknown. In the study, we established an *in vitro* oxidative stress model using ethanol-exposed human gastric mucosal epithelial (GES-1) cells. We found that CAP pretreatment effectively mitigated ROS levels and preserved mitochondrial integrity. Proteomic analysis indicated a significant enrichment of antioxidant-associated pathways. Intriguingly, CAP augmented NRF2 protein expression and facilitated its nuclear translocation, thereby amplifying the transcription and translation of downstream antioxidant response elements (ARE), such as HO-1, NQO1, Trx and GSS. These observations were congruent in hydrogen peroxide-exposed mesenchymal stem cells, which indicates the universality of its antioxidant ability. Furthermore, CAP was found to inhibit the KEAP1-NRF2 interaction, and it failed to trigger the activation of NRF2 after KEAP1 knockout in 293T. CAP specifically interacts with the Kelch domain of KEAP1 and binds to allosteric sites. To enhance drug safety, we also formulated and characterized IR-HSA@CAP nanoparticles. *In vivo* assessments corroborated that CAP markedly curtailed ROS and invigorated the NRF2/ARE pathway. Additionally, CAP modulated inflammatory markers, reducing IL-1β, TNF-α, IL-6, and CXCL1/KC(IL-8), while elevating IL-10 in gastric tissues. Given that the non-covalent binding modality of natural compounds to KEAP1 remains underreported, CAP may emerge as a pioneering direct inhibitor of the KEAP1-NRF2 interaction.

Keywords

BLI; Co-IP; pull-down; interaction

1 Introduction

Ethanol (EtOH), commonly referred to alcohol in everyday life, is a fascinating ingredient found in beer, wine, and liquor. Excessive drinking poses great health risks and causes about 3 million deaths per year[1]. Alcohol causes oxidative damage to gastric mucosa. Persistent and intensified oxidative stress, particularly reactive oxygen species (ROS), induces DNA damage, protein oxidation, and lipid peroxidation[2]. Subsequently, it causes gastrointestinal dysfunction, chronic atrophic gastritis, and is closely related to the occurrence of gastric cancer[3].

Natural products are key sources of drugs or lead compounds for treating major diseases[4].Previous reports have shown that the incidence rate of gastric ulcer in Indians and Malaysians is quite low. Chili peppers appear more frequently in the cuisine of these two countries[5]. This raises doubts about whether chili peppers can alleviate gastric mucosal damage and further alleviate gastric ulcers. Currently, experiments conducted in rats have demonstrated that red pepper/capsaicin (CAP) has significant protective effects on ethanol-induced gastric mucosal damage[6,7]. However, the underlying mechanism is largely unknown.

The key transcription factor, Nuclear Factor erythroid 2-Related Factor 2 (NRF2), is conventionally anchored in the cytoplasm by its binding partner, Kelch-like ECH-associated protein 1 (KEAP1). And the KEAP1-NRF2 signaling pathway is a fundamental line of defense against oxidative challenges[8]. Several NRF2 agonists, like mangiferin, inhibits both the transcription and translation of KEAP1, resulting in NRF2 accumulation[9]. In contrast, activators such as t-BHQ and curcumin have been shown to disrupt the KEAP1-NRF2 complex, thereby preventing the degradation of NRF2[10,11]. Contemporary research indicates that judicious activation of the KEAP1-NRF2 axis can

decelerate the disorders closely associated with oxidative stress[12]. More researchers focused on the development of non-covalent binding agents with KEAP1, which represents lower side effects and higher commercial value.

In this study, ethanol induced acute oxidative damage models were established *in vitro* and *in vivo*, and the effects of CAP pretreatment on KEAP1/NRF2/ARE signaling cascade were verified. Conclusively, CAP may emerge as a pioneering direct inhibitor of the KEAP1-NRF2 interaction, which also offering an in-depth understanding of its antioxidative defense mechanism.

2 Results

2.1 Capsaicin protects GES-1 from oxidative stress

The molecular formula of CAP (Compound CID: 1548943) is provided in **Supplemental Figure 1a**. Initially, an oxidative stress model was established in human gastric mucosal epithelial (GES-1) cells due to the significant generation of reactive oxygen species (ROS) following ethanol (EtOH) treatment. A dose-dependent decline in cell viability upon exposure to EtOH was observed, with viability decreasing to approximately 50% after 1.5 hours of treatment with 5% EtOH **(Supplemental Figure 1b)**. To evaluate the protective effects of CAP, GES-1 model cells with pretreated with CAP for 2.5 hours before introducing EtOH. Results revealed that a pretreatment with 8 μM CAP significantly enhanced cell viability to 93.84% **(Supplemental Figure 1c)**. Notably, further increases in CAP concentration did not augment the protective effect, possibly due to cytotoxicity at higher concentrations[13]. When the CAP concentration exceeded 100 μM, cell viability dramatically decreased to below 10% **(Supplemental Figure 1d)**. Then, three CAP concentrations (2, 8, and 32 μM) and three EtOH concentrations (0.5%, 3.5%, and 5%) on GES-1 were further valuated to establish a stable cell model *in vitro* **(Supplemental Figure**

1e-g). Moreover, we assessed EtOH-induced apoptosis and found that the percentage of apoptotic cells was reduced from 28.85% to 13.95% in the group pretreated with 8 μM CAP, compared to the EtOH-only group **(Supplemental Figure 1h)**.

Then the morphological changes in GES-1 cells were examined. Cells in the EtOH-only group displayed a rounded morphology and showed a marked tendency for aggregation. We observed a significant amount of cell detachment from the culture plate's substrate. In contrast, cells that were pretreated with 2 μM and 8 μM CAP demonstrated improved adhesion to the substrate and largely retained their characteristic cellular shape **(Figure 1a)**. To explore whether CAP's restorative effects on GES-1 cellular morphology were linked to its mitigation of oxidative stress, we assessed reactive oxygen species (ROS) production using DCFH-DA staining. The EtOH-only group exhibited elevated levels of ROS, as indicated by increased green fluorescence, while the phenomenon was substantially diminished in CAP-pretreated groups **(Figure 1b)**. Flow cytometric analyses further corroborated this trend, revealing that intracellular ROS levels consistently declined (from 83.1±3.59% to 60.23±12.67% and finally to 48.9±5.55%) with incremental dosages of CAP (0, 2, and 8 μM) **(Figure 1c and 1d)**. To evaluate the impact of CAP on intracellular redox homeostasis, the activity of superoxide dismutase (SOD) ,as well as the amount of malondialdehyde (MDA) were measured, the latter being a byproduct of membrane lipid peroxidation. Our findings demonstrated that SOD levels were significantly upregulated following CAP treatment **(Figure 1e)**, while MDA production was markedly reduced **(Figure 1f)**. Collectively, these results suggest that CAP effectively attenuates ROS levels and modulates redox balance in GES-1 cells exposed to EtOH.

2.2 Capsaicin activates the NRF2/ARE signaling pathway

With analytical techniques such as network pharmacology[14] and single-cell sequencing, researchers identified pivotal target proteins implicated in the precursory lesions of gastric cancer[15]. Based on the network targets analysis, CAP played a networked and modular role, including pathways and biological processes related to ROS, inflammation and immune **(Figure 1g)**. However, the specific mechanism of ROS regulation by CAP is still unclear, so we carried out proteomic analyses to identify differentially expressed genes (DEGs). A comprehensive overview of these DEGs is presented in the heat map. Utilizing stringent criteria for statistical significance (Fold change ≥ 1.2, P value ≤ 0.05), Compared DEGs between the CAP-pretreated group and the EtOH-only group, analysis revealed that 120 proteins were significantly up-regulated, while 65 were down-regulated following CAP treatment **(Supplementary Figure 2a)**. Subsequent Gene Ontology (GO), and Kyoto Encyclopedia of Genes and Genomes (KEGG) enrichment analyses were performed on this pool of 185 DEGs **(Supplementary Figure 2b and 2c)**. As anticipated, the top-ranked terms in the 'Molecular Function' category of the GO analysis included 'antioxidant activity' (GO: 0016209) and 'oxidoreductase activity' (GO: 0016491). Genes corresponding to these functional categories were highlighted in the volcano plot **(Supplemental Figure 2d)** and annotated in the heat map **(Figure 1h)**. Intriguingly, our findings demonstrated a significant elevation in the expression of key antioxidant-related proteins, such as glutathione synthase (GSS), superoxide dismutase 1 (SOD1), and thioredoxin (TXN, also known as Trx). These proteins are associated with previously reported antioxidant response elements (AREs) and function as downstream targets of the transcription factor NRF2[16]. Based on these insights, we hypothesized that CAP may activate the NRF2/ARE signaling pathway.

To substantiate the hypothesis, we conducted western blot experiments and discovered that CAP notably augmented the expression levels of NRF2 and

heme oxygenase 1 (HMOX1, also known as HO-1) in GES-1 cells **(Figure 1i)**, which is a downstream gene regulated by NRF2. Concurrently, the elevated expression levels of GSS and Trx proteins, which are also downstream targets of NRF2, further validated by the proteomic analysis **(Figure 1j)**. A grayscale quantification of these pivotal proteins was elaborated in **Supplementary Figure 2e-h**. Recognizing NRF2's role as a transcriptional regulator, we further scrutinized the transcript levels of these essential target genes: TXN, HMOX1, and NQO1. It's worth mentioning that NAD(P)H quinone dehydrogenase 1 (NQO1) is also a classic target gene of NRF2[17]. Quantitative reverse transcription PCR (RT-qPCR) assays demonstrated that 8 μM of CAP significantly amplified the transcription of these antioxidant-associated genes **(Figure 1k)**.

In a parallel experiment involving a hydrogen peroxide (H_2O_2)-induced oxidative stress model in human umbilical cord mesenchymal stem cells (UC-MSC), CAP pretreatment similarly boosted the transcription and protein expression levels of NRF2 and its downstream genes of TXN, HMOX1, and NQO1 **(Figure 1l and 1m)**. A grayscale quantification of these pivotal proteins was also elaborated in **Supplementary Figure 2i and 2j**. These collective findings suggest that CAP's role in ROS mitigation is not confined to a specific cell type.

2.3 Capsaicin promotes NRF2 to translocate into nucleus

To examine the impact of CAP on the role of NRF2 as a transcription factor, we proceeded to investigate its subcellular localization following CAP pretreatment. Our findings revealed that a concentration of 8 μM CAP effectively facilitated the translocation of NRF2 into the nucleus. Specifically, 52.29% of NRF2 fluorescence was co-localized with the nuclear dye DAPI, as determined by analyses across three randomly selected fields of view for each sample group **(Figure 2a and 2b)**. To corroborate this observation, we

conducted a nucleoplasm separation assay to quantify the expression levels of NRF2 in both the nuclear and cytoplasmic compartments **(Figure 2c)**. Grayscale analysis of the immunoblotting data further corroborated that the nuclear accumulation of NRF2 augmented with increasing concentrations of CAP treatment **(Figure 2d)**.

2.4 Capsaicin inhibits the degradation of NRF2

NRF2 is known to undergo proteasomal degradation, so we employed PS-341, a renowned proteasome inhibitor, to selectively impede the 20S proteasome. Our data revealed that PS-341 independently elevated NRF2 expression levels. Moreover, when cells were co-incubated with both PS-341 and CAP, the overall NRF2 levels rose even further, which suggesting a synergetic effect of CAP and PS-341 on inhibiting NRF2 degradation and the mechanism of CAP may differ from that of PS-341 **(Figure 2e)**.

To delve deeper into whether CAP influences the degradation phase of protein synthesis, we utilized actinomycin (CHX), a recognized inhibitor of protein synthesis[18]. As shown in **Figure 2f**, CHX treatment led to a rapid decline in NRF2 protein levels, making it nearly undetectable approximately 30 minutes after addition. Conversely, NRF2 levels remained noticeably stable when co-incubated with CAP, implying that CAP may prolong the half-life of NRF2. These findings strengthen the notion that CAP boosts NRF2 stability by hindering its proteolytic degradation. In alignment with existing literature, which posits that K48 ubiquitination facilitates NRF2 degradation[19, 20], we carried out ubiquitin immunoprecipitation experiments. These indicated a modest reduction, approximately 17.57%, in NRF2 K48 ubiquitination following CAP treatment **(Figure 2g and 2h)**.

2.5 Capsaicin protects mitochondrial function

The mitochondria serve as the primary intracellular source of ROS,

predominantly via the mitochondrial respiratory chain[21]. Initial exploratory studies focused on NRF2's role in maintaining mitochondrial integrity[22]. Our findings revealed a 21.76% decrease in average mitochondrial branch length following EtOH treatment. Remarkably, CAP pretreatment appeared to preserve the structural integrity of the mitochondria in GES-1 cells, with indices nearly indistinguishable from the control group **(Figure 2i and 2j)**. We subsequently turned our attention to the mitochondrial membrane potential (MMP, ΔΨm), a key factor in sustaining mitochondrial oxidative phosphorylation and the subsequent production of adenosine triphosphate (ATP). Exposure to 5% EtOH for 10 minutes or to the positive control CCCP for 20 minutes led to comparable declines in ΔΨm, affecting approximately 30% of cells. Notably, pretreatment with 8 μM CAP ameliorated this reduction in ΔΨm **(Figure 2k and 2l)**.

Typically, diminished levels of ATP serve as a hallmark of compromised mitochondrial function. To investigate this, we employed a luminescence detector to quantify both extracellular and intracellular ATP concentrations. The extracellular ATP levels surged to approximately three times in EtOH-only group than those of the control, while a corresponding sharp decrease was observed in intracellular ATP concentrations **(Supplementary Figure 3a)**. In striking contrast, CAP pretreatment effectively stabilized intracellular ATP levels, maintaining them at 96.65% of their original concentration **(Supplementary Figure 3b)**. Building on these observations, we assessed the end product of the glycolytic pathway, lactate (LA), as well as the transcription levels of key metabolic enzymes—pyruvate kinase M2 (PKM2) and lactate dehydrogenase A (LDHA). CAP treatment resulted in significant downregulation of both LA and the aforementioned enzymes, suggesting a potential metabolic reprogramming from glycolysis to oxidative phosphorylation **(Supplementary Figure 3c-3f)**. Previous studies have demonstrated that CAP can directly bind to and inhibit the activity of PKM2 and

LDHA, subsequently attenuating inflammatory responses[23]. Therefore, our findings highlighted the role of CAP in maintaining mitochondrial function and further reducing oxidative stress.

2.6 CAP disrupts KEAP1-NRF2 interaction

In the cytoplasm, KEAP1 serves as a crucial adaptor protein for E3 ubiquitin ligases, facilitating the ubiquitination and subsequent proteasomal degradation of NRF2. To explore the possible influence of CAP on NRF2 stabilization via KEAP1 modulation, we conducted a comprehensive analysis of KEAP1's mRNA and protein expression levels under CAP treatment. Intriguingly, our findings revealed no significant alterations in KEAP1 expression, both at the transcriptional **(Figure 3a)** nor the protein levels **(Figure 3b)**. Possibility given that CAP exerted no impact on KEAP1 expression, it suggested the likelihood that CAP may disrupt the molecular interaction between KEAP1 and NRF2.

Surface plasmon resonance (SPR) was used to quantitatively evaluate the *in vitro* binding affinity between purified KEAP1 and NRF2. The observed dissociation constant (K_D) for the KEAP1-NRF2 complex was calculated to be 1.14 ± 0.15 nM **(Figure 3c)**, corroborating earlier reports of a strong association between these two proteins[24]. Upon exposing KEAP1 to increasing concentrations of CAP—ranging from 16 μM to 500 μM—a consistent, dose-dependent decrease in KEAP1-NRF2 binding was noted **(Figure 3d)**. We further substantiated these observations through co-immunoprecipitation (Co-IP) assays. Treatment with 32 μM CAP led to a 52.79% reduction in the endogenous NRF2 associated with KEAP1 within cellular models **(Figure 3e and 3f)**. Collectively, these results presented the first empirical evidence that CAP effectively impairs the KEAP1-NRF2 interaction.

2.7 Knockout of KEAP1 affects the action of CAP

To investigate whether KEAP1 functions as a key target for the antioxidant properties mediated by CAP, KEAP1-knockout (KO) 293T cell lines was generated and performed validation studies using western blot **(Supplementary Figure 4a)**. Initially, we observed that CAP significantly activated the NRF2/HO-1 pathway in wild-type 293T cells, leading to a pronounced increase in cell viability **(Figure 3g and 3h).** This finding was consistent with observations made in GES-1 and UC-MSC cells. However, in KEAP1-KO cells, an innate resilience to oxidative stress was evident, likely due to the constitutive activation of endogenous NRF2 and its downstream effector, HO-1. As a result, the CCK8 assay revealed no significant differences in cell viability between the groups **(Figure 3i)**, corroborating previous studies that KEAP1-KO mice exhibited reduced oxidative stress and inflammatory responses[25]. Importantly, in the KEAP1-KO 293T cell line, CAP displayed a reduced ability to activate NRF2 and HO-1 **(Figure 3j)**. A grayscale quantification of these pivotal proteins was elaborated in **Supplementary Figure 4b-4e.** All Taken together, our findings strongly supported the notion that KEAP1 serves as a crucial mediator for the antioxidant effects conferred by CAP, and played a pivotal role in amplifying the NRF2/ARE signaling pathway.

2.8 Capsaicin directly interacts with KEAP1

As previously documented, small molecules categorized as NRF2 agonists, such as Dimethyl fumarate (DMF), curcumin, and sulforaphane, predominantly target and inhibit KEAP1 function[26]. To probe the interplay between KEAP1 and CAP within a cellular environment, we conducted cellular thermal shift assay (CETSA). In the absence of CAP, KEAP1 experienced marked degradation within a temperature window of 58°C to 67°C. In contrast, the presence of CAP significantly stabilized KEAP1 against thermal denaturation, resulting in noticeably sustained levels of the KEAP1 protein in cells **(Figure 4a)**.

To probe the specific CAP-binding sites on KEAP1, we utilized computational docking and all-atom simulations, to map the positioning of possible CAP-interacting residues within the surface pockets of KEAP1, with particular focus on the Kelch domain responsible for NRF2 interaction **(Figure 4b and Supplementary Figure 5a)**. The most energetically favorable model demonstrated that the vanillyl headgroup of CAP was inserted into the Kelch channel, while its flexible hydrocarbon chain remained at the periphery of the NRF2-Kelch interface. Based on this docking model, we hypothesized that the CAP binding pocket partially overlapped with the KEAP1-NRF2 interacting interface **(Figure 4c)**. Hence, we modeled interactions between NRF2 and Kelch in the presence of CAP using all-atom molecular dynamics simulations. When CAP associated with Kelch, the NRF2-Kelch complex was disrupted **(Supplementary Figure 5b and 5c and supplementary videos 1 and 2)**. Indeed, for the NRF2-Kelch complex, the average distance between NRF2 Asp29 and Keap1 Arg415 kept around 1.20 nm, indicating stable bindings throughout the 100 ns trajectory. For the NRF2-CAP-Kelch complex, however, the average distance fluctuated to 2.87 nm, resulting in dissociated NRF2 around the Kelch domain **(Supplementary Figure 5d and 5e)**. Our simulations corroborated with the experimental observation that CAP can function as protein-protein interface inhibitors.

Interestingly, the majority of previously identified KEAP1 inhibitors are known to enact covalent modifications on the cysteine residues of KEAP1, thereby disrupting the interactions between KEAP1-Cul3 and KEAP1-NRF2, and consequently activating the downstream NRF2/ARE signaling pathway[27]. Therefore, we introduced the reducing agent dithiothreitol (DTT) into the cell culture. Existing literature suggests that KEAP1's active cysteines can be covalently altered by electrophilic agents like CN-2F, and such modifications are generally reversible in the presence of DTT[18]. Additionally, the

effectiveness of catechol moieties in NRF2 activation is often neutralized by pre-treatment with DTT[28]. However, our results indicated that the CAP-induced elevation of NRF2 expression levels was not inhibited by DTT **(Figure 4d)**.

To further investigate whether CAP also forms covalent bonds with key cysteine residues on the KEAP1 surface, we targeted our scrutiny towards the functionally critical cysteines, such as Cys151, Cys273 and Cys288[29]. Employing tandem mass spectrometry (MS/MS), we assessed the molecular weights of KEAP1 samples following incubation with CAP and found no evidence of CAP-induced modifications **(Figure 4e, and Supplementary Figure 6a-6d)**. These results suggested that although CAP bound directly to KEAP1, it did not do so through covalent interaction.

2.9 CAP specifically interacts with the Kelch domain of KEAP1

To investigate the impact of CAP on the binding affinity between the Kelch domain and NRF2, we conducted immunoprecipitation (IP) and pull-down analysis using purified Kelch-domain-only proteins. The IP results revealed a noticeable reduction in NRF2 proteins bound to the Kelch domain, corresponding with incremental concentrations of CAP. In parallel, the levels of unbound NRF2 in the supernatant progressively increased **(Figure 4f and Supplementary Figure 6e)**. Further substantiating these observations, commercial purified NRF2 proteins were also used. Pull-down assays furnished compelling empirical evidence that CAP effectively disrupted the direct interaction between the Kelch domain and NRF2 **(Figure 4g)**.

2.10 CAP binds KEAP1 at allosteric sites

According to the results of molecular docking and dynamic simulation, we purified both the wild type Kelch domain (WT) and the mutated variant (Mut) of KEAP1 proteins. The mutated version involved substitutions at residues

Y334A, R380A, N382A, N414A, R415A, Y572A, and S602A (the orthostatic site), which are residues reported to engage NRF2 and classic Keap1 inhibitors. Bio-Layer Interferometry (BLI) revealed that the binding affinity between CAP and the Kelch domain (WT) was 31.45 μM with R^2=0.99 **(Figure 5a**). Intriguingly, the mutated Kelch domain (Mut) exhibited diminished, but still appreciable, affinity for CAP with a K_D of 102.4 μM with R^2=0.98 **(Figure 5b).** Our biophysical examinations suggested the orthostatic NRF2-binding pocket was not entirely responsible for CAP-binding. Indeed, the Kelch (Mut)-Flag protein failed to pull down any NRF2 from cellular lysates, but it still interacted with CAP **(Figure 5c)**. These collective findings suggest that the CAP-binding pocket and the NRF2-binding interface on KEAP1 may be different from each other, implicating CAP as an allosteric modulator of KEAP1. This specificity may arise from the interaction between the vanillyl headgroup of CAP and the main chain atoms of the Kelch domain, which appears to be largely unaffected by NRF2 binding **(Figure 5d)**. The crystal structures depicting the binding sites between previously identified ligands and the Kelch protein (PDB: 4IQK and 5FNQ) were illustrated on the left-hand side of **Figure 5e**. In contrast, the right-hand side revealed our discovery of the binding sites between CAP and the Kelch protein, which were very inconsistent with previous reports. These insights suggested that CAP could potentially represent a novel class of NRF2 agonists.

2.11 Preparation and characterization of IR-HSA@CAP

Encouraged by the discovery of CAP as a new agonist of NRF2, we developed a convenient nano-drug delivery platform for the efficient utilization of CAP *in vivo*. We opted for Human Serum Albumin (HSA) as the encapsulating material, given its FDA-approved status for superior biocompatibility and an excellent safety profile. HSA has also been documented to offer protective effects to the gastric mucosa[30]. As a fluorescent marker, we employed IRDye800, a widely-used near-infrared fluorescent dye in biomedical research

for applications such as protein tagging and advanced imaging. Utilizing these components, we successfully formulated CAP-encapsulated IRDye800-HSA nanoparticles, denoted as IR-HSA@CAP **(Figure 6a)**. The labeling ratio stood at 1.48 (IRDye800: HSA) and achieved a coupling efficiency of 93.29% **(Figure 6b)**, and the encapsulation was notably efficient through calculation[31].

The structural attributes of the IR-HSA@CAP nanoparticles were meticulously characterized using transmission electron microscopy (TEM), the results of which were illustrated in **Figure 6c**. Subsequent analysis via dynamic light scattering (DLS) provided insights into the hydrated particle size and Zeta-potential of these nanoparticles. Notably, the size distributions of HSA@CAP and IR-HSA@CAP nanoparticles were remarkably consistent. The former exhibited an average particle size of 139.27 ± 7.49 nm **(Figure 6d)**, while the latter registered at approximately 160.97 ± 14.78 nm **(Figure 6e)**. In terms of Zeta-potential, the HSA@CAP nanoparticles displayed an increase to -4.16 ± 0.78 mV post-formation, as compared to native HSA, which had a potential of -15.45 ± 1.40 mV. Interestingly, this Zeta-potential returned to a value of -10.55 ± 0.50 mV upon integration with IRDye800 in the IR-HSA@CAP nanoparticles, thereby substantiating the effective binding of the dye **(Figure 6f)**.

To assess the biocompatibility and endocytic uptake of IR-HSA@CAP nanoparticles, we employed GES-1 and Raw264.7 cell lines as *in vitro* models. Importantly, no discernible decline in cell viability was observed over a 24-hour period, underscoring the non-cytotoxic nature of the nanoparticles **(Supplementary Figure 7a and 7b)**. Furthermore, intracellular fluorescence intensity escalated progressively with time, reaching a point where nearly all cells exhibited IR-Dye800 positivity within just one hour **(Figure 6g)**. These findings strongly implied that the IR-HSA@CAP nanoparticles were rapidly internalized by cells and exhibit commendable biocompatibility.

To precisely quantify the CAP content in IR-HSA@CAP nanoparticles, we established a standard curve for CAP using high-performance liquid chromatography (HPLC) at a wavelength of 282 nm **(Supplementary Figure 7c)**. To evaluate the stability and release profile of the nanomaterials under gastrointestinal conditions, we examined the release kinetics of CAP in normal saline (SPSS, pH=7.0) and simulated gastric fluid (SGF, pH=2.0). Preliminary tests revealed that virtually all encapsulated CAP could be rapidly liberated in the SGF environment **(Supplementary Figure 7d and 7e)**. In subsequent animal trials calibrated to the actual concentrations of CAP, we found that the CAP concentration in SGF swiftly attained a theoretical value of 1 mg/ml within 30 minutes, while remaining essentially constant in SPSS conditions **(Figure 6h and 6i)**. These findings collectively suggest that IR-HSA@CAP nanoparticles were capable of achieving rapid release of CAP in the gastric milieu to a notable extent.

2.12 IR-HSA@CAP NPs activated the Nrf2/ARE signaling pathway *in vivo*

To investigate the protective effects of IR-HSA@CAP nanoparticles against EtOH-induced gastric mucosal injury *in vivo*, Sprague-Dawley rats were systematically allocated into eight distinct experimental groups: Group A served as the control group and received normal saline (SPSS); Group B was administered CAP alone (CAP); Group C received IR-HSA@CAP nanoparticles (IR-HSA@CAP); Group D was treated with ethanol (EtOH); Group E was pre-treated with CAP before EtOH exposure (CAP + EtOH); Group F was similarly pre-treated, but with IR-HSA@CAP nanoparticles (IR-HSA@CAP + EtOH); Group G received Human Serum Albumin (HSA) as a pretreatment prior to EtOH administration (HSA + EtOH); and Group H was pre-treated with Rebamipide prior to EtOH exposure (Rebamipide + EtOH). Rebamipide was selected as the positive control due to its known capacity to activate the Nrf2 signaling pathway[32].

The *in vivo* experimental protocol unfolded as follows: To ensure gastric emptying, rats were subjected to a 24-hour fasting period. Subsequently, they were administered SPSS, CAP, or the designated treatment in accordance with their group allocation. After a 45-minute pretreatment phase, the rats were exposed to 75% EtOH for an additional 1.5 hours. Following this, the animals were humanely euthanized, and the gastric tissue samples were collected for subsequent experiments and analyses. Precise dosages administered were as follows: CAP at 1 mg/kg, HSA at 2 mg/kg, and Rebamipide at 100 mg/kg. The HSA@CAP nanoparticles used were prepared to contain 1 mg/kg of CAP and 2 mg/kg of HSA, as quantified by HPLC.

To elucidate the spatiotemporal distribution of CAP within the rat model, imaging was conducted at various time intervals post-administration. The data revealed that CAP was predominantly processed through the gastrointestinal tract, exhibiting notable localization within the stomach **(Figure 6j and 6k)**.

The administration of either CAP or IR-HSA@CAP alone did not result in noticeable damage to the gastric tissues, in contrast to the control group. However, significant hemorrhaging and erosion were evident in gastric tissues exposed to EtOH **(Figure 7a, left)**. Utilizing the Guth scoring system, we quantitatively assessed the Gastric Mucosa Ulcer Injury (UI) index. The average UI index in the EtOH group soared to 36.0, signifying acute tissue damage. On the other hand, remarkable reductions in the UI index were observed in both the CAP and IR-HSA@CAP pretreatment groups, registering at 7.0 and 5.3 respectively. These levels were roughly on par with the Rebamipide group, which had a UI index of 9 **(Figure 7a, right)**. These findings align well with our expectations. Notably, the effective dose of CAP (1 mg/kg) was substantially lower than that of Rebamipide (100 mg/kg), underscoring the potential advantages of CAP. Additionally, while the

HSA-pretreated group did exhibit some attenuation of gastric mucosal injury, the reduction was not statistically significant (UI=17.7). This suggested that CAP was the principal active component responsible for the observed effects in the IR-HSA@CAP nanoparticles.

Subsequently, we quantified the extent of pathological damage using H&E staining coupled with the Masuda scoring system, wherein a higher index reflects more severe tissue damage. The pathological damage index registered at 6.3 in the EtOH-only group, while the HSA-treated group showed a slightly lower index at 4.7. The CAP-treated group further reduced this index to 3.7. Remarkably, the employment of either IR-HSA@CAP nanoparticles or Rebamipide led to a substantial decline in pathological damage, with both treatments registering an identical index of 1.7 **(Figure 7b)**. These results demonstrate that the therapeutic efficacy of IR-HSA@CAP nanoparticles surpassed that of either CAP or HSA administered individually. Specifically, the reduction in tissue damage was 1.77-fold greater than that achieved with CAP alone and 2.88-fold greater compared to HSA alone.

To evaluate the capability of CAP to inhibit the EtOH-induced augmentation of ROS levels in gastric tissues *in vivo*, we conducted dihydroethidium (DHE) staining on cryo-sectioned gastric specimens. Utilizing the red fluorescence emission as a biomarker for ROS levels, we discerned a marked elevation in the EtOH-treated and HSA-pretreated groups relative to the control. In stark contrast, pre-treatment with either CAP or IR-HSA@CAP nanoparticles substantially mitigated ROS production, with reductions of 45.42% and 36.99% respectively, compared to the EtOH-only group **(Figure 7c)**. Concurrently, MDA assays underscored that IR-HSA@CAP nanoparticles efficaciously curtailed lipid peroxidation levels in the gastric tissues by an approximate 72.82% **(Figure 7d)**. Additionally, CAT activity in the tissues was bolstered by 31.85% following treatment with IR-HSA@CAP nanoparticles (**Figure 7e)**.

Further molecular investigation involving reverse transcription quantitative polymerase chain reaction (RT-qPCR) assays disclosed that CAP treatment markedly elevated the expression levels of intracellular HMOX1 and NQO1 genes, approximating a twofold increase **(Figure 7f)**.

Subsequently, we scrutinized the modulatory effects of IR-HSA@CAP on the Nrf2/ARE signaling pathway. Our findings, substantiated through immunohistochemistry **(Figure 8a-8c)** and western blot analyses **(Supplementary Figure 8j-8m)**, revealed that pre-treatment with IR-HSA@CAP led to a significant upregulation of Nrf2 expression. Concurrently, IR-HSA@CAP pre-treatment also stimulated elevated expression levels of HO-1 and Trx. These collective observations suggest that IR-HSA@CAP was capable of orchestrating the Nrf2/ARE signaling axis, thereby providing a rapid and effective modulatory mechanism for oxidative stress and homeostatic balance. To delve deeper into the anti-inflammatory potential of our treatment strategy, we analyzed homogenized gastric tissue samples for the expression profiles of various chemokines and inflammatory mediators. Intriguingly, pre-treatment with either CAP or IR-HSA@CAP elicited a marked suppression in the expression levels of pro-inflammatory cytokines such as IL-1β, TNF-α, IL-6, and CXCL1, while simultaneously augmenting the expression of the anti-inflammatory cytokine IL-10 **(Figure 8d).** Not surprisingly, IR-HSA@CAP played a better anti-inflammatory effect**.** The novel mechanism of capsaicin nanoparticles in preventing EtOH-induced gastric mucosal injury is shown in **Figure 8e**.

Finally, we assessed the biosafety of IR-HSA@CAP in rats through continuous oral administration over a one-week period **(Supplementary Figure 8a)**. No significant alterations were observed in the organ indices for either the liver or spleen (**Supplementary Figure 8b and 8c)**. Comprehensive blood biochemical analyses further revealed that varying concentrations of

IR-HSA@CAP exerted no deleterious impact on hepatic function, as indicated by levels of ALT, AST, and T-Bil **(Supplementary Figure 8d-f)**, or on renal function, as evidenced by measurements of BUN, CRE, and UA **(Supplementary Figure 8g-i)**. These collective findings underscore the high biosafety profile of the IR-HSA@CAP nanoparticles.

3 Discussion

CAP, a natural small molecule derived from chili peppers, has been identified and verified to modulate the KEAP1-NRF2-ARE pathway in our study. This pathway is a promising therapeutic target for combatting free radical damage associated with numerous conditions, including Alzheimer's disease[33], chronic kidney disease[34], cardiovascular disease[35], cancer and aging[36]. Over the past few decades, the scientific community has tirelessly sought molecules capable of activating NRF2. Hu et al. reported the first small-molecule inhibitor of the Keap1-Nrf2 PPI from a high-throughput screen (HTS) in 2013[37]. Davies and co-workers began with a crystallographic screen of approximately 330 fragments and developed KI-696 as a nanomolar Keap1-Nrf2 PPI inhibitor[38,39]. A spectrum of NRF2 agonists, both natural and synthetic, covalent and non-covalent, have been unveiled. However, Kim T. Tran et al. reported that many compounds are difficult to synthesize and the binding activity of half of the compounds cannot be demonstrated convincingly[40]. Practical application faces two primary challenges. First and foremost, covalent modifications to KEAP1 pose a noteworthy concern regarding "off-target" effects owing to their electrophilic properties. These effects have the potential to impact various other cellular proteins, impeding their commercial success[26]. Furthermore, unregulated activation of NRF2 can inadvertently foster cancer progression by shielding malignant cells and bolstering their proliferation, metastatic potential, and resistance to therapeutic interventions[41].

Recent advancements have been geared towards the development of direct inhibitors for the KEAP1-NRF2 interaction, drawing significant attention from the scientific community[42]. Interestingly, our research unequivocally identifies the non-covalent interaction between CAP and KEAP1. Dimethyl fumarate (DMF), a KEAP1-dependent NRF2 agonist, has progressed positively in phase III clinical trials. The recognition that DMF's minimal side effects stem from its dual mode of action—both covalently modifying reactive cysteines and non-covalently activating NRF2 via the Kelch domain of KEAP1—has marked a pivotal milestone in the development of drugs targeting KEAP1[26]. We found that at lower concentrations, CAP effectively bound with the Kelch domain **(Figure 5a and 5c)** and activated NRF2, subsequently promoting the expression of downstream antioxidant genes **(Figure 1i-1m)**. *In vivo* studies, we observed almost no adverse reactions **(Supplementary Figure 8).** Additionally, Merritt, J.C. et al. reported that CAP at high concentrations possesses potent anti-cancer properties[43]. This aligns with our CCK8 experimental findings that heightened CAP concentrations curtailed cell viability **(Supplementary Figure 1c and 1d)**. The duality of pharmacological impact of CAP remains a topic of discussion. The interplay and mechanisms between CAP's varying modes in both regular and cancerous cells, which underlie its antioxidant and anticancer actions, are intricate and warrant further exploration.

Notably, to date, no natural product has been confirmed as a direct inhibitor of the KEAP1-NRF2 interaction. In our findings, the dissociation constant (K_D) between CAP and Kelch was reported as 262 ± 0.15 μM **(Figure 5a)**, a relatively weak association compared with ML334 (K_D=1 μM) and some synthetically designed peptides[44]. However, the KEAP1-NRF2 interaction was significantly inhibited by CAP **(Figure 3d and 3e)**. Of particular significance and surprise, our investigation revealed that CAP and Kelch establish

interactions at allosteric sites. Notably, the Kelch mutant protein failed to engage with NRF2 **(Figure 5e)**, yet it maintained its interaction with CAP **(Figure 5b and 5d)**. Computational simulations indicated that this specificity might stem from the interaction between the vanillyl headgroup of CAP and the main chain atoms within the Kelch domain, which seemed largely unaffected by NRF2 binding. This phenomenon stands as distinct when compared to other known NRF2 agonists, as depicted in **Figure 5f and 5g**. Our comprehensive analysis of the CAP-KEAP1 binding dynamics, particularly the unique mode of interaction with Kelch, offers valuable insights for the development of innovative NRF2 activators.

Nonetheless, several concerns warrant further examination. The impact of CAP on the gastric mucosa, as evidenced in animal studies, is contingent upon its dosage and duration of administration. A low dose of CAP applied short-term can mitigate indomethacin-induced gastric microhemorrhage. Conversely, a high dose applied prophylactically over an extended period does not confer this benefit [45, 46, 47]. It was similarly observed in our studies, where the effective concentration window for natural CAP is a little narrow. For individuals with pre-existing gastric conditions, the epithelial cells of the gastric mucosa might exhibit heightened sensitivity to CAP. This not only diminishes its protective capability but might also exacerbate ulcer severity.

Concurrently, the IR-HSA@CAP NPs we employed demonstrated prompt gastric release *in vivo*, underscoring the superior attributes of nanomedicine. This could amplify the antioxidant and anti-inflammatory potency of CAP, thereby resulting in enhanced therapeutic outcomes. Yet challenges persist, not least the inability to achieve a treatment that targets the stomach exclusively. Considering ongoing research into nanomaterials for CAP, there's scope to further refine CAP's delivery strategy from a pharmacological

standpoint.

In summary, the present study provides evidence that CAP effectively mitigates oxidative stress through the activation of NRF2 and its non-covalent binding to KEAP1's Kelch domain. The unique binding site between CAP and Kelch sets it apart from the commonly reported small molecule inhibitors, hinting at its potential as a novel class of NRF2 agonists. Moving forward, the development of derivatives inspired by CAP holds promise as a compelling avenue for the creation of therapeutic agents aimed at attenuating oxidative damage.

4 Materials and methods

Reagents and chemicals

Capsaicin (CAP) used *in vitro* was purchased from Solarbio Life Science (CAS:404-86-4, Cat No. IC0060). CAP used *in vivo* was purchased from MCE (Cat No. HY-10448). The anhydrous ethanol (EtOH) was purchased from Tianjin Jiangtian Chemical Technology Co. LTD in China (CAS:64-17-5, Cat No.268). Primary antibodies of anti-HA-Tag (Cat No. AE008), anti-Strep II-Tag (Cat No. AE066) and anti-MYC-Tag (Cat No. AE010) were purchased from ABclonal Technology. The primary antibody to anti-Flag (Cat No. 80010-1-RR), anti-Actin (catalog no. 66009-1-Ig), anti-GAPDH (Cat No. 60004-1-Ig), anti-NRF2(Cat No. 16396-1-AP), anti-GSS (Cat No. 15712-1-AP), anti-HMOX1(Cat No. 10701-1-AP) anti-Trx (Cat No. 14999-1-AP) and anti-KEAP1(Cat No. 10503-2-AP) were purchased from Proteintech. Anti-HA affinity matrix (Cat No. 11815016001) was purchased from Roche. Anti-Flag affinity matrix (catalog no. A2220) and albumin from human serum (HSA, Cat No. A3782) was purchased from Sigma. The FITC Goat anti-Rabbit IgG (H+L) was purchased from SIMUBIOTECH (Cat No. S2003). Reactive Oxygen Species Assay Kit (Cat No. CA1410), DAPI (Cat No. H-1200) and the CCK-8

cell proliferation and cytotoxicity assay kit (Cat No. CA1210) were acquired from Solarbio Life Science. The enhanced chemiluminescence (ECL) reagent (Cat No. SQ201) was obtained from EpiZyme. HSA Cycloheximide (CHX, Cat No. HY-12320), DTT (Cat No. HY-15917) and Bortezomib (PS-341, Cat No. HY-10227) were purchased from MCE. Human KEAP-1 Protein was bought from Sino Biological (Cat No.11981-HNCB). Recombinant human Nrf2 protein was bought from Abcam (Cat No. ab132356). IRDye® 800CW was bought from *LI-COR.*

Cell lines and cell culture

Human gastric mucosal epithelial cells (GES-1), HEK293T human embryonic kidney 293 cells (293T) and Human umbilical cord mesenchymal stem cells (UC-MSC) were obtained from the American Type Culture Collection (ATCC) and cultured at 37°C in 5% CO_2. KEAP1 Knockout 293T Cell Lysate (293T-KO) was purchased from ABclonal (RM02350). 293T and 293T-KO were maintained in Dulbecco's modified Eagle's medium (DMEM) supplemented with 10% fetal bovine serum (FBS) and 1% penicillin-streptomycin (100 IU/mL). GES-1 and UC-MSC were maintained in Roswell Park Memorial Institute 1640 medium (RPMI-1640), supplemented with 10% fetal bovine serum (FBS) and 1% penicillin-streptomycin (100 IU/mL), RAW 264.7 also needs an additional 1%Glutamax. The cell passage ratio was 1:2-1:4, every 2-3 days.

Plasmid construction

The plasmids of pCDNA3.1-KEAP1-FLAG (Cat No. P8893) and pCMV-NFE2L2 (human)-HA-Neo (Cat No. P45110) were purchased from the platform of MiaoLingPlasmid (http://www.miaolingbio.com/). In order to better express NRF2 in 293T, we inserted the NFE2L2 (human)-HA into EcoRV/Xba□ of VR1012 through the pEASY®-Basic Seamless Cloning and Assembly Kit purchased from Transgen Biotech (Cat No. CU201-02). The plasmid of Ub-K48-Myc and the no-load plasmids of pcDNA3.1 and VR1012

are available in our own laboratory. The Kelch domain of KEAP1(Lys312-Cys624)[48] was downloaded and then the optimized (for Escherichia coli; Homo sapiens) sequence was cloned into the vector of pET-28a (+) by adding 5' (NdeI) and 3' (XhoI), so the plasmid of kelch in pET-28a(+) was constructed from the company of Azenta. At the same time, a Kelch plasmid with mutation at 7 sites (R415A, N382A, R380A, N414A, S602A, Y334A and Y572A) was designed, which was also synthesized directly using the same method described above.

CCK-8 cell viability and cytotoxicity assay

GES-1 cells cultured in 96-well plates were used for CCK8 experiments. After the cells had been cultured for more than 24 hours and spread all over the bottom of the plate (10^4 cells/ml), the experiments were carried out. The cells were washed twice with PBS, low, medium and high concentrations of ethanol (EtOH) were added into the medium of 1640 (0.5%, 3.5% and 5% v/v) and cultured for 1.5 h at 37°C in 5% CO_2. After the 1.5 h, carefully discard the supernatant before slowly adding the well diluted CCK8 solution, and the absorbance at 450 nm was measured using a microplate reader according to the manufacturer's instructions. To identify the effective concentration of CAP , CAP dissolved in DMSO (original concentration of 50 mM) was diluted to the specified concentration in 1640 medium(2, 4, 8, 16 and 32 μM), mixed well and added to the cells for 2.5 h. and then added the corresponding concentration of EtOH directly for another 1.5 h. After a total of 4 hours of treatment, CCK8 cell viability was measured according to the above method. UC-MSC cells was treated like GES-1, only using 200 μM H_2O_2 to replace EtOH. What's more, in order to judge the safety of nanomaterials, HSA@CAP NPs including HSA (0.04 mg/ml) and CAP (0.02 mg/ml) were added into GES-1 and Raw264.7 cells for 24 hours and then the cytotoxicity assay was conducted same as the tests for cell viability.

Effect of CAP and EtOH on the morphology of GES-1

GES-1 cells with good condition were cultured in 24-well plates at a concentration of 5 × 10^5/well. Then, 5% EtOH was added in the EtOH group and the cells pre-added with 2 μM or 8 μM of CAP were termed as the “2 μM CAP + EtOH” group and the“8 μM CAP + EtOH” group. Cell morphology of each group was observed under the fluorescence microscope using only the bright field**.** In subsequent cell experiments, we also adopted the same modeling method and set such four groups, hereinafter referred to as the model construction of this experiment.

Flow cytometry of apoptosis

GES-1 cells cultured in 6-well plates were used for detecting apoptosis. Annexin V-FITC Apoptosis Detection Kit (Solarbio Life Science) was used to determine the cell apoptosis rate according to the manufacturer's instructions. In 6-well plates, GES-1 cells were seeded. The treatment of the cells was consistent with that of the morphological examination. Then, we washed them with cold PBS three times and used a cell scraper to carefully collect cells in each group before staining with Annexin V-FITC and PI at room temperature (RT) for 15 min. Finally, flow cytometry was used to detect apoptotic cells using a FACS flow cytometer (BD Biosciences, USA). The results were analyzed by FlowJo software (version 10.8.1, TreeStar, USA).

ROS detection

For testing the intracellular ROS, 10^6 GES-1 cells were cultured on a 12-well plate and placed in an incubator at 37 °C under 5% CO_2. After CAP pretreatment for 2.5 h and EtOH incubation for 1.5 h, the intracellular ROS level was measured. 1 ml of DCFH-DA (10 μM) was added and incubated in the dark at 37 °C for 30 min. Then, we collected cells and washed them with

PBS three times, and finally, the ROS activity was detected by inverted fluorescence microscope and flow cytometry. For the detection of ROS in gastric tissue, five micrometers cryosections of frozen gastric tissues were stained with 10 μM Dihydroethidium (DHE) for 30 min in the dark at RT. Pictures were taken at 200-fold magnification and quantification by Ipp6. 0.

Measurements of MDA, SOD and CAT

GES-1 cells with good condition were cultured in 6-well plates. After the four groups described above are constructed, the cells were collected and counted, and detected by chemiluminescence according to the kit instructions. For in vitro cell experiments, the cells were collected into the centrifuge tube, and then the supernatant was discarded after centrifugation. 1 mL extraction solution was added for every 5 million cells and ultrasonic crushing was performed (power 200 w, ultrasonic 3 s, interval 10 s, repeat 30 times). Centrifuge 8000 g at 4 °C for 10 minutes, take supernatant and put it on ice for test. Gastric tissue of each rat was homogenized in freshly prepared ice cold 0.05□M potassium phosphate buffer (pH 7.4) with 20 times dilution. The supernatant was obtained by centrifuging the tissue homogenate at 15,000□×g at 4 °C for 10 min, which was used for the evaluation of the gastric MDA level, SOD and CAT activities, and the results were expressed as nmol/mg protein or U/mg protein. SOD activity was determined using a SOD assay Kit (BC0175, Solarbio, China); CAT activity was evaluated using a CAT assay (BC0205, Solarbio, China) and the MDA level was also determined by a MDA assay (BC0025, Solarbio, China).

Mitochondrial staining and branch length analysis

After different treatments on GES-1 lived on slippers in a 48-well plate, MitoTracker Red CMXRos (M9940, Solarbio, China) was added to the medium, followed by incubation at 37 °C for 15 min. The culture medium was then

discarded and the cells washed gently three times with PBS and fixed in 4% paraformaldehyde for 30 min. Images were obtained under a fluorescence microscope. Finally, cells were stained with DAPI for 10 min, washed three times with ddH_2O, and then imaged under a fluorescence microscope (Nikon). Quantitative analysis of the mean branch length of mitochondria was calculated using MiNA software (https://github.com/ScienceToolkit/MiNA) developed by ImageJ.

Detection of mitochondrial membrane potential (MMP, $\triangle\Psi m$)

After the treatment, $\triangle\Psi m$ of GES-1 cells were measured with a mitochondrial membrane potential detection kit (CA1310, Solarbio, China). In detail, after pretreatment with capsaicin for 2.5 h, cells were treated with 5% EtOH for 10 min or CCCP, a positive control reagent in the kit, for 20 min. Cells were collected and incubated in a cell incubator at 37 °C with JC-10 staining solution for 20 min. Then, we followed the instructions of the kit and analyzed it by flow cytometry.

ATP detection

After pretreatment with capsaicin for 2.5 h, GES-1 cells were treated with 5% EtOH for 10 min, ATP in cell supernatant and intracellular were detected using an ATP test kit (S0026, Beyotime, China). The principle of the kit is that ATP is needed to generate fluorescence when firefly luciferase catalyzed luciferase. The fluorescence production is detected by the chemiluminescence instrument, which is proportional to the concentration of ATP within a certain range.

Lactic acid (LA) detection

After CAP pretreatment for 2.5 h and EtOH incubation for 1.5 h, the intracellular LA level was measured using a Lactic Acid assay kit (A019-2-1,

Nanjing Jiancheng Bioengineering Institute, China). Follow the kit instructions and test at 530 nm (EnSpire Multilabel Reader).

Network targets analysis of CAP

Network targets analysis was performed to obtain the potential mechanism of effects of CAP on ROS[49-51]. Biological effect profile of CAP was predicted based our previous network-based algorithm：drugCIPHER[52-58]. Enrichment analysis was conducted based on R package clusterProfiler v4.9.1 and pathways or biological processes enriched with significant P value less than 0.05 (BH adjustment) were remained for further studies. Then pathways or biological processes related to ROS and significantly enriched were filtered and classified into three modules, including ROS, inflammation and immune. Network targets of CAP against ROS were constructed based on above analyses.

Proteomics and omics analysis

GES-1 cells were divided into three groups: Ctrl; EtOH and CAP + EtOH. After the cells were treated respectively, they were washed with PBS and 300 μl SDT lysis solution was added into a 10 cm petri dish. In order to obtain the differential expression genes (DEGs) , this project adopted the quantitative proteomics technology of TMT, which mainly included two stages of mass spectrometry experiment and data analysis. The DEGs were enriched by GO and KEGG through the DAVID database (https://david.ncifcrf.gov/) , and the bioinformatic analysis was performed using the OmicStudio tools at https://www.omicstudio.cn/tool.

Western blotting

At the specified time after processing, the cells and supernatant were collected directly into the centrifuge tube. After centrifugation at 6,500 rpm for 5 min,

cells were washed three times with PBS and lysed in RIPA buffer. The protein samples were separated by 12% SDS-PAGE (80 V, 30 min and 130V, 55min), transferred to nitrocellulose(100 V, 105 min), sealed with 5% skim milk (30 min at RT) , probed with the indicated primary antibodies (overnight at 4 °C), washed 3 times with TBST (120 rpm,6 min) and exposed to species-specific horseradish peroxidase (HRP)-conjugated secondary antibodies(60 rpm, 60 min). After washed 3 times with TBST, immunoreactive bands were visualized by enhanced chemiluminescence. The gray value of protein was analyzed by ImageJ software. GAPDH and ACTB served as the reference for equivalent total protein volume. WB of rat tissue was operated on ice at 4 °C during the whole process. The tissue was cut into fine fragments and the high efficiency RIPA tissue lysate (R0010, Solarbio, China) was added at the ratio of 200 ul lysate per 20 mg gastric tissue. The lysate was homogenized with a glass homogenizer until fully lysed. After centrifuging at 12000 rpm for 5 min, the supernatant was taken to conduct subsequent target protein detection.

Quantitative PCR (RT-qPCR)

Total RNA from the cells was extracted using a QIAzol lysis reagent. The RNA was reverse-transcribed into cDNA using TransScript first-strand cDNA synthesis supermix according to the manufacturer's instruction (AE301-02, TransGen Biotech, China). Hieff UNICON® Universal Blue qPCR SYBR Green Master Mix was used for qPCR (11184ES03, Yeasen , China) . The relative amount of target gene mRNA was normalized to that of *GAPDH* mRNA in the same sample. The primers' sequences used in cell experiments were designed through PrimerBank (https://pga.mgh.harvard.edu/primerbank/) and the primers' sequences of PKM2 and LDHA were designed through a reference[59]. The sequence of qPCR primers in the rat experiments were listed

using *r-ACTB* and etc. All the primer sequences of RT-qPCR were listing in **Table 1**.

Table 1：**The primer sequences of RT-qPCR**

Genes	Forward Sequences (5'-3')	Reverse Sequences (5'-3')
GAPDH	GAA GGT GAA GGT CGG AGT C	GAA GAT GGT GAT GGG ATT TC
GSS	GGG AGC CTC TTG CAG GAT AAA	GAA TGG GGC ATA GCT CAC CAC
HMOX1	AAG ACT GCG TTC CTG CTC AAC	AAA GCC CTA CAG CAA CTG TCG
NQO1	GAA GAG CAC TGA TCG TAC TGG C	GGA TAC TGA AAG TTC GCA GGG
TXN	GTG AAG CAG ATC GAG AGC AAG	CGT GGC TGA GAA GTC AAC TAC TA
KEAP1	CTG GAG GAT CAT ACC AAG CAG G	GGA TAC CCT CAA TGG ACA CCA C
PKM2	GTG CCG CCT GGA CAT TGA CTC	ATT CAG CCG AGC CAC ATT CAT CC
LDHA	GCT CAT CGT CTC AAA CCC AGT GG	ACT CCC AGC CTT TCT CCC ATC AG
r-ACTB	GAA GTG TGA CGT TGA CAT CCG	TGC TGA TCC ACA TCT GCT GGA
r-NQO1	AAG CGT CTG GAG ACT TCT GGG	CCT CTG GCG AAG AAA CTC TG
r-HMOX1	AAG AGG CTA AGA CCG CCT TC	GCA TAA ATT CCC ACT GCC AC

Immunofluorescence staining and confocal microscopy

At the indicated times of treatment with CAP and EtOH, GES-1 cells were fixed in 4% paraformaldehyde (PFA) for 15 min, permeabilized with 0.5% Triton X-100 for 10 min, blocked with 1% bovine serum albumin (BSA) for 20 min, and then probed with specific antibodies (dilution ratio of the primary antibody of Nrf2, 1:100; secondary antibody, 1:500). Then, 10 mg/mL DAPI was used to label nuclei. Images were captured with a confocal laser scanning microscope system. The colocalization of signals from two channels was detected using ImageJ software.

Nucleoplasm separation

After different treatments on GES-1 cultured in 6-well plates , cells were centrifuged at 6000 rpm for 5 min and discarded the supernatant. All subsequent operations were performed on ice at 4 °C. First, the cells were decomposed for 5 min by adding 100ul of cytoplasmic lysate (containing 10 mM HEPES ,10 mM KCl ,0.1 mM EDTA, 0.5% NP-40 and adding extra 1:1000 PMSF and 1:2000 DTT). Then blow 200 times with a 200 ul Eppendorf. After centrifugation at 500 g for 5 min, the supernatant was the cytoplasmic lysate. Finally, 200 ul of NP40-free lysate was added for nuclear washing and precipitation for 3 times (discard the supernatant). After mixing with an oscillator, the mixture was centrifuged at 500 g for 5 min to obtain the nuclear proteins. All samples were boiled at 99 °C for 10 min for WB.

Coimmunoprecipitation (Co-IP)

First, 3 mg pcDNA3.1 or Keap1-FLAG plasmid with polyethylenimine (PEI) reagent was transfected into 293T cells (5×10^6 cells/ml). After 24 h, the cells were treated with 32 μM capsaicin for 2.5 hour and then suspended with phosphate-buffered saline (PBS) and centrifuged at 6,500 rpm for 5 min to collect cell precipitate. The cells were lysed in 700 ml lysis buffer (50 mM Tris-HCl, pH = 7.5, 150 mM NaCl, and 0.5% Triton-100), and the lysates were incubated with anti-FLAG affinity matrix at 4 °C for 10 h. The lysates were washed six times with PBS, eluted with glycine buffer (pH = 2), boiled in SDS loading buffer, and analyzed by WB. For the ubiquitin experiment, 3 mg Ub-K48-Myc and 3 mg VR1012 or Nrf2-HA plasmids with PEI were co-transfected into 293T. After 36 h, the cells were treated with 32 μM capsaicin for 2.5 h. The rest of the steps were the same except that anti-HA affinity matrix was used.

Pull-down

Purified Kelch-Strep protein (10 μg) was incubated with 10 μL of specific

anti-Strep affinity matrix for a duration of 4 hours at 4°C. Solutions containing 500 μM and 1000 μM CAP were prepared, and 1 μg of NRF2 protein was added to each reaction system. The reaction systems were further incubated at 4°C for another 2 hours. Subsequently, the unbound proteins were subjected to wash steps consistent with Co-IP procedures, followed by result assessment through Western Blot experiments.

The degradation of Nrf2

To test the degradation of Nrf2, the drugs CHX and PS-341 were used. GES-1 cells were incubated with or without 32 μM CAP for 3 h, followed by treatment with CHX (50 μg/mL) for 15 min or 30 min. Total cell lysates were collected and analyzed by WB for total Nrf2 protein expression. What's more, GES-1 cells were incubated with or without PS-341(100 nM) and CAP (32 μM) for 3 h to compare the activation of Nrf2 between co-incubation and single drug use. The total amount of Nrf2 was quantified with ImageJ.

Surface plasma resonance（SPR）

When the Human KEAP-1 Protein was fixed on the metal surface of the chip as a ligand protein, the mobile phase containing the analytical substance (NRF2 or Capsaicin) flowed through the stationary phase. The experiment was conducted in strict accordance with the relevant standard procedures of SPR. The analysis software used for the results of this experiment was TraceDrawer (Ridgeview Instruments ab, Sweden), and the analysis method was One to One analysis model. The design of experimental methods and parameters involved are shown in **Table 1**:

Table 2：**Experimental method design and parameters**

Project details	
Ligand	Human KEAP-1 Protein

Analyte	Capsaicin、NRF2	
Running buffer	PBS (pH7.4),1%DMSO PBS (pH7.4)	
Regeneration solution	10 mM Glycine-HCl	
Association and dissociation flow rate	20 μl/min, Association 240 s, Dissociation 360 s	
Temperatures	25 °C	
Sensor Chip	Sensor Chip COOH	Nicoya
OpenSPR	OpenSPRTM	Nicoya

Bio-layer interferometry assay (BLI)

The Octet RED96e system (Molecular Device, ForteBIO) is ideally suited for the characterization of protein-small molecule binding kinetics and binding affinity. The protein Kelch (WT)-His and Kelch (Mut)-His were purified and diluted to 30-50 μg/mL. The proteins were then immobilized on Ni-NTA sensors. The sensors were then blocked, washed and moved into wells containing various concentrations of the test compound of CAP in kinetic buffer. Program settings default to programs that bind proteins and small molecules in the system. The binding signals were identified and the results were analyzed using the OctetHT V10.0 software. R^2 is an estimate of the goodness of fit with values close to 1 indicating an excellent fit.

Cellular thermal shift assay (CETSA)

GES-1 cells on 24-well plates were treated with 1640 medium containing Capsaicin (32 μM) or 0.1%DMSO for 2.5-3 h. Cells were collected from each group and divided into seven PCR tubes on average. The cells were heated at the specified temperature (46-67 °C) for 3 min and cooled at room temperature. The cells were lysed with liquid nitrogen and freeze-thawed four times. The cell lysates were centrifuged at 12000 rpm for 30 min at 4 °C. The protein supernatant was analyzed by WB, and was quantified by ImageJ software.

Mass spectrometry (MS-MS)

The final concentration of capsaicin was 50 μM (DMSO less than 0.5% by volume) after 20 μg Keap1 protein solution was added with 2 μl capsaicin (1 mM) and was dissolved in HEPES (pH=7.4). Incubate at 30 °C for 2 h in the dark. Separated by 10% SDS-PAGE gel (80 V 30 min and 130 V 20 min); The overexpressed KEAP1 was detected by Coomassie Bright Blue staining, and the corresponding bands were removed from the gel for intra-gel digestion as described. In short, the gel tablets were reduced with DTT (10 mM) and alkylated with iodoacetamide (50 mM). The rest of the process is followed and the digested protein samples are manipulated and analyzed by Novogene Co. Ltd., China.

Computational simulations

The flexible docking between the KEAP1 Kelch domain and the small molecule CAP was performed by RosettaLigand[60]. The crystal structure of Kelch (PDB: 3WN7) and 3D model of CAP (ZINC1530575, https://zinc.docking.org/substances/ZINC000001530575/) were used as the input structures. The Rosetta software was obtained from https://www.rosettacommons.org and version number is 2021.36+release.57ac713 57ac713a6e1d8ce6f60269b3988b1adac1d96fc6. Rosetta Transform mover with the box size of 8.0 Å was used for global searching and the HighResDocker mover was used for fine tuning the binding positions. 1000 docking poses were generated and the interface binding energies was calculated using the default Ref2015_wts score functions. The docking results were ranked by the binding energy and clustered for the representative conformations.

The 100 ns all-atom simulations on the complex of NRF2-KEAP1 or

NRF2-CAP-KEAP1 were performed with the Gromacs 2019.6 package[61]. The initial poses of inhibitor-binding conformations were adopted from the docking results and from PDB 3WN7. The system was solvated in a box (81 ´ 81 ´ 81 Å3) with TIP3P waters and 0.15 M NaCl. The CHARMM36 force field was adopted, wherein the topologies of inhibitors were generated by the CHARMM_GUI Ligand Modeler[62]. The energy minimizations were performed to relieve unfavorable contacts, followed by 10 ns equilibration steps. Subsequently, the simulations were performed at 300 K (velocity-rescale thermostat) and constant pressure (1 bar, Parrinello-Rahman NPT ensemble). The nonbonded interaction cut-off for electrostatics calculations was set as 10 Å and the particle mesh Ewald (PME) method was used for calculation of long-range electrostatic interactions. LINCS constraints were applied to h-bonds and the time step was 2 fs. Throughout the trajectories, the representative binding conformations were clustered based on their structural similarities.

Protein purification

The synthetic cDNA encoding Kelch (WT) and Kelch (Mut) were cloned into pET28a vector respectively. The plasmid vectors were transformed into E. coli BL21 (DE3) to express proteins, which were induced by 0.4 mM isopropyl β-D-1-thiogalactopyranoside (IPTG) at 16°C for 18 hours, followed by cultured at 37 °C until the OD600 value reached 0.6. The cells were isolated by centrifugation, resuspended and lysed in lysis buffer. The lysates were centrifuged for 60 min at 12,000 rpm to obtain the supernatant. Gravity flow purification of the proteins in the supernatant were obtained using Ni-affinity chromatography and eluted in buffer containing 200 mM imidazole. The final proteins were purified and validated by Superdex 75 10/300GL resin.

Preparation of IR-HSA@CAP NPs

500 μl CAP (20 mg/ml) was uniformly injected into 10 ml of HSA solution (2

mg/mL), and stirred for 10 min at 700-800 rpm/min at RT. 50% glutaraldehyde was diluted 100 times and 80 μl was injected into the flask. Keep stirring at the same speed for 3 h. After termination of reaction, dialysis bag was used overnight to remove excess glutaraldehyde. HSA@CAP NPs were obtained and stored at 4 °C under shading. To obtain IR-HSA@CAP NPs, we added 40 μl of IRDye800 (5 mg/ml) into 700 μl of HSA@CAP NPs (2 mg/ml HSA). After incubation at RT for 1 h, the solution was added with a 30 KDa protein concentration tube, and centrifuged at 12000 rpm for 5 min. Some of the unbound antibody probes were centrifuged. Then eluted 4-5 times with 1XPBS (0.01 M) until there was no color in the collection tube. Protein concentration and labeling (DOL) were determined by measuring absorption at 280 nm and 780 nm.

Particle size and Zeta potential

The morphology of the prepared IR-HSA@CAP NPs was observed by Transmission Electron Microscopy (TEM, TECNAI G2 F20). The sample was prepared as follows: IR-HSA@CAP NPs were diluted 150 times before ultrasonic treatment, so that the particles were evenly distributed in the solution. 10 μl sample solution was slowly dropped onto the surface of the copper mesh, covered with a protective cover to prevent dust pollution in the air, and waited for the sample solvent to fully volatilize at RT. The hydration particle size and potential of the samples were measured using Litesizer™ 500. 2-3 ml of aqueous solution diluted 1000 times by HSA@CAP and IR-HSA@CAP NPs were added into the plastic sample plate, and the hydration particle size and potential were detected at 25 °C. The same sample was measured at least three times in parallel to calculate the mean.

High Performance Liquid Chromatography (HPLC)

The peak time and area corresponding to the HPLC were used to calculate the capsaicin content in IR-HSA@CAP. HPLC procedure: sample size was 10 μl,

the temperature of C18 was adjusted to 30 °C, acetonitrile (10% - 94%) and 0.1% phosphoric acid water were used as mobile phase and time range was 0~28 min. To evaluate the release of capsaicin in simulated gastric fluid (SGF : 3.2 g pepsin, 2 g NaCl, 7 ml Concentrated hydrochloric acid in 1L ddH_20, pH=2.0), 200 μl of evenly mixed IR-HSA@CAP was added to 800 μl of freshly configured SGF/SPSS, and mixed at 37 °C. At the corresponding time point, it was evenly mixed with anhydrous methanol at 1:1 and added 1 ml mixed solution into an injection bottle for measurement.

Endocytosis and *in vivo* imaging of IR-HSA@CAP NPs

In vivo experiments, healthy adult male Sprague-Dawley (SD) rats, weighing 230-260 g were used. The newly prepared IR-HSA@CAP NPs solution was diluted and added into the medium, and incubated with GES-1 cells for 1 h, 2 h and 3.5 h. After the supernatant was discarded, the cells were washed with PBS for 5 times, and the ICG fluorescence in the cells was detected by APC-Cv7-A channel of flow cytometry. SD rats (24 h after fasting) were given 1 ml IR-HSA@CAP NPs by intragastric administration. The fluorescence signals of rats were detected after administration. At the same time, images of side position were photographed at 45 min and 60 min, and dissected major organs (heart, liver, spleen, lung and kidney) and digestive system (stomach, large intestine, colon and duodenum) *in vitro* to determine the specific location of CAP.

Pathological examination of gastric tissue (H&E Staining)

As previously mentioned, the stomach tissue is soaked in 4% paraformaldehyde tissue fixation solution for 24 h. Then the stomach tissue was cleaned, dehydrated by different concentrations of ethanol solution, transparent in xylene, and finally embedded in paraffin. Sections of 3 μm thickness were prepared, dried and dewaxed, stained with hematoxylin and

eosin (H & E), dehydrated and sealed, and any structural changes were detected microscopically (OLYMPUS, DP26).

Detection of cytokines in gastric tissue (ELISA)

Interleukin (IL)- 1β, IL-6 , CXCL1/KC(IL-8), IL-10 and tumor necrosis factor-alpha(TNF-α) levels in the gastric tissue lysate were determined to assess gastric inflammation. ELISA kits from Solarbio, catalogue numbers SEKR-0002, SEKR-0005, SEKR-0014, SEKR-0006 and SEKR-0009 were used for IL-1β , IL-6, CXCL1, IL-10 and TNF-α, respectively following the manufacturer's instructions.

Statistical analysis

All results were analyzed with GraphPad Prism Version 9 and are presented as mean values ± SD. Statistical significance was determined using Student's T test. Statistical significant was indicated at a P value < 0.05. (ns, no significance; *, $P < 0.05$; **, $P < 0.01$; ***, $P < 0.001$; ****, $P < 0.0001$).

Ethics statement

All animal research procedures were followed in accordance with the standards set forth in the eighth edition of Guide for the Care and Use of Laboratory Animals (published by the National Academy of Sciences, The National Academies Press, Washington, D.C.), and was approved by the Animal Care Committee of the Faculty of Medicine, Tianjin University (Approval No: TJUE-2023-238).

Acknowledgements

This work was financially supported by National Natural Science Foundation of China (T2341008 and 22077094) and Key Research Project of the 14th

Five-Year Plan for Cancer Prevention and Treatment at Tianjin Cancer Institute (No. YZ-08).

Conflict of interests

The authors declare no competing interests.

Data availability

The data used to support the findings of this study are included within the article.

Contributions

Xiaoning Gao: experiments, methodology, data analysis and writing-original draft; Bo Zhang, Peiyuan Liu, Liren Liu and Zixiang Liu: conceptualization, methodology, data curation and resources; Mingyue Yuwen, Ruyang Tan and Junli Ba: experiments and visualization; Boyang Wang, Zhiru Yang , Xue Bai, Shama Shiti and Cong Tang: resources and data analysis; Kairui Liu: writing-polish; Tao Wang and Cheng Zhu: investigation, data curation and writing-review; Shao Li: conceptualization, resources and funding acquisition; Jun Kang: conceptualization; supervision; writing-original draft; funding acquisition; writing-review and editing.

References

1 Organization, W. H. *Global status report on alcohol and health 2018: executive summary*, <https://www.who.int/publications/i/item/a-summary-of-the-global-status-report-on-alcohol> (2018).

2 Zhang, H. *et al.* Anthocyanin supplementation improves anti-oxidative and anti-inflammatory capacity in a dose-response manner in subjects with dyslipidemia. *Redox biology* **32**, 101474, doi:10.1016/j.redox.2020.101474 (2020).

3 Yu, S. *et al.* Protective Effect of Polyphenols Purified from Mallotus oblongfolius on Ethanol-Induced Gastric Mucosal Injury by Regulating Nrf2 and MAPKs Pathways. *Antioxidants (Basel, Switzerland)* **11**, doi:10.3390/antiox11122452 (2022).

4 Srinivasan, K. Antioxidant potential of spices and their active constituents. *Critical reviews in*

1149 *food science and nutrition* **54**, 352-372, doi:10.1080/10408398.2011.585525 (2014).
1150 5 Satyanarayana, M. N. Capsaicin and gastric ulcers. *Critical reviews in food science and*
1151 *nutrition* **46**, 275-328, doi:10.1080/1040-830491379236 (2006).
1152 6 Holzer, P., Livingston, E. H., Saria, A. & Guth, P. H. Sensory neurons mediate protective
1153 vasodilatation in rat gastric mucosa. *The American journal of physiology* **260**, G363-370,
1154 doi:10.1152/ajpgi.1991.260.3.G363 (1991).
1155 7 Saeki, T. *et al.* Mechanism of prevention by capsaicin of ethanol-induced gastric mucosal
1156 injury--a study in the rat using intravital microscopy. *Alimentary pharmacology & therapeutics*
1157 **14 Suppl 1**, 135-144, doi:10.1046/j.1365-2036.2000.014s1135.x (2000).
1158 8 Lee, J. S. & Surh, Y. J. Nrf2 as a novel molecular target for chemoprevention. *Cancer letters*
1159 **224**, 171-184, doi:10.1016/j.canlet.2004.09.042 (2005).
1160 9 Song, J. *et al.* Mangiferin activates Nrf2 to attenuate cardiac fibrosis via redistributing
1161 glutaminolysis-derived glutamate. *Pharmacological research* **157**, 104845,
1162 doi:10.1016/j.phrs.2020.104845 (2020).
1163 10 Anuranjani & Bala, M. Concerted action of Nrf2-ARE pathway, MRN complex, HMGB1 and
1164 inflammatory cytokines - implication in modification of radiation damage. *Redox biology* **2**,
1165 832-846, doi:10.1016/j.redox.2014.02.008 (2014).
1166 11 Rahban, M., Habibi-Rezaei, M., Mazaheri, M., Saso, L. & Moosavi-Movahedi, A. A. Anti-Viral
1167 Potential and Modulation of Nrf2 by Curcumin: Pharmacological Implications. *Antioxidants*
1168 *(Basel, Switzerland)* **9**, doi:10.3390/antiox9121228 (2020).
1169 12 Hybertson, B. M., Gao, B., Bose, S. K. & McCord, J. M. Oxidative stress in health and disease:
1170 the therapeutic potential of Nrf2 activation. *Molecular aspects of medicine* **32**, 234-246,
1171 doi:10.1016/j.mam.2011.10.006 (2011).
1172 13 Thongin, S. *et al.* Beneficial effects of capsaicin and dihydrocapsaicin on endothelial
1173 inflammation, nitric oxide production and antioxidant activity. *Biomedicine &*
1174 *pharmacotherapy = Biomedecine & pharmacotherapie* **154**, 113521,
1175 doi:10.1016/j.biopha.2022.113521 (2022).
1176 14 Li, S. *Network pharmacology*. (Springer, 2021).
1177 15 Zhang, P. *et al.* Dissecting the Single-Cell Transcriptome Network Underlying Gastric
1178 Premalignant Lesions and Early Gastric Cancer. *Cell reports* **27**, 1934-1947.e1935,
1179 doi:10.1016/j.celrep.2019.04.052 (2019).
1180 16 Ngo, V. & Duennwald, M. L. Nrf2 and Oxidative Stress: A General Overview of Mechanisms
1181 and Implications in Human Disease. *Antioxidants (Basel, Switzerland)* **11**,
1182 doi:10.3390/antiox11122345 (2022).
1183 17 Xiang, Q., Zhao, Y., Lin, J., Jiang, S. & Li, W. The Nrf2 antioxidant defense system in
1184 intervertebral disc degeneration: Molecular insights. *Experimental & molecular medicine* **54**,
1185 1067-1075, doi:10.1038/s12276-022-00829-6 (2022).
1186 18 Liu, X. F. *et al.* Developing dietary curcumin mono-carbonyl piperidinone analogs as
1187 Nrf2-dependent cytoprotectors against oxidative damage: Structure-activity relationship and
1188 mechanisms. *Free radical biology & medicine* **186**, 66-75,
1189 doi:10.1016/j.freeradbiomed.2022.05.009 (2022).
1190 19 Zhang, Q. *et al.* DUB3 deubiquitinates and stabilizes NRF2 in chemotherapy resistance of
1191 colorectal cancer. *Cell death and differentiation* **26**, 2300-2313,
1192 doi:10.1038/s41418-019-0303-z (2019).

1193 20 Hong, Z. *et al.* Celastrol targeting Nedd4 reduces Nrf2-mediated oxidative stress in astrocytes
1194 after ischemic stroke. *Journal of pharmaceutical analysis* **13**, 156-169,
1195 doi:10.1016/j.jpha.2022.12.002 (2023).
1196 21 Dan Dunn, J., Alvarez, L. A., Zhang, X. & Soldati, T. Reactive oxygen species and mitochondria:
1197 A nexus of cellular homeostasis. *Redox biology* **6**, 472-485, doi:10.1016/j.redox.2015.09.005
1198 (2015).
1199 22 Esteras, N. & Abramov, A. Y. Nrf2 as a regulator of mitochondrial function: Energy metabolism
1200 and beyond. *Free radical biology & medicine* **189**, 136-153,
1201 doi:10.1016/j.freeradbiomed.2022.07.013 (2022).
1202 23 Zhang, Q. *et al.* Capsaicin ameliorates inflammation in a TRPV1-independent mechanism by
1203 inhibiting PKM2-LDHA-mediated Warburg effect in sepsis. *Cell chemical biology* **29**,
1204 1248-1259.e1246, doi:10.1016/j.chembiol.2022.06.011 (2022).
1205 24 Yamamoto, M., Kensler, T. W. & Motohashi, H. The KEAP1-NRF2 System: a Thiol-Based
1206 Sensor-Effector Apparatus for Maintaining Redox Homeostasis. *Physiological reviews* **98**,
1207 1169-1203, doi:10.1152/physrev.00023.2017 (2018).
1208 25 Zhao, W. *et al.* Astrocytic Nrf2 expression protects spinal cord from oxidative stress following
1209 spinal cord injury in a male mouse model. *Journal of neuroinflammation* **19**, 134,
1210 doi:10.1186/s12974-022-02491-1 (2022).
1211 26 Unni, S., Deshmukh, P., Krishnappa, G., Kommu, P. & Padmanabhan, B. Structural insights into
1212 the multiple binding modes of Dimethyl Fumarate (DMF) and its analogs to the Kelch domain
1213 of Keap1. *The FEBS journal* **288**, 1599-1613, doi:10.1111/febs.15485 (2021).
1214 27 Lu, M. C., Ji, J. A., Jiang, Z. Y. & You, Q. D. The Keap1-Nrf2-ARE Pathway As a Potential
1215 Preventive and Therapeutic Target: An Update. *Medicinal research reviews* **36**, 924-963,
1216 doi:10.1002/med.21396 (2016).
1217 28 Lin, D., Dai, F., Sun, L. D. & Zhou, B. Toward an understanding of the role of a catechol moiety
1218 in cancer chemoprevention: The case of copper- and o-quinone-dependent Nrf2 activation by
1219 a catechol-type resveratrol analog. *Molecular nutrition & food research* **59**, 2395-2406,
1220 doi:10.1002/mnfr.201500297 (2015).
1221 29 Saito, R. *et al.* Characterizations of Three Major Cysteine Sensors of Keap1 in Stress Response.
1222 *Molecular and cellular biology* **36**, 271-284, doi:10.1128/mcb.00868-15 (2016).
1223 30 Wu, Y. *et al.* Iodinated BSA Nanoparticles for Macrophage-Mediated CT Imaging and Repair of
1224 Gastritis. *Analytical chemistry* **93**, 6414-6420, doi:10.1021/acs.analchem.0c05407 (2021).
1225 31 Bhattacharyya, S. *et al.* Synthesis and biological evaluation of panitumumab-IRDye800
1226 conjugate as a fluorescence imaging probe for EGFR-expressing cancers. *MedChemComm* **5**,
1227 1337-1346, doi:10.1039/c4md00116h (2014).
1228 32 Moon, S. J. *et al.* Rebamipide suppresses collagen-induced arthritis through reciprocal
1229 regulation of th17/treg cell differentiation and heme oxygenase 1 induction. *Arthritis &*
1230 *rheumatology (Hoboken, N.J.)* **66**, 874-885, doi:10.1002/art.38310 (2014).
1231 33 Osama, A., Zhang, J., Yao, J., Yao, X. & Fang, J. Nrf2: a dark horse in Alzheimer's disease
1232 treatment. *Ageing research reviews* **64**, 101206, doi:10.1016/j.arr.2020.101206 (2020).
1233 34 Guerrero-Hue, M. *et al.* Protective Role of Nrf2 in Renal Disease. *Antioxidants (Basel,*
1234 *Switzerland)* **10**, doi:10.3390/antiox10010039 (2020).
1235 35 Reuland, D. J., McCord, J. M. & Hamilton, K. L. The role of Nrf2 in the attenuation of
1236 cardiovascular disease. *Exercise and sport sciences reviews* **41**, 162-168,

1237 doi:10.1097/JES.0b013e3182948a1e (2013).
1238 36 Schmidlin, C. J., Dodson, M. B., Madhavan, L. & Zhang, D. D. Redox regulation by NRF2 in
1239 aging and disease. *Free radical biology & medicine* **134**, 702-707,
1240 doi:10.1016/j.freeradbiomed.2019.01.016 (2019).
1241 37 Hu, L. *et al.* Discovery of a small-molecule inhibitor and cellular probe of Keap1-Nrf2
1242 protein-protein interaction. *Bioorganic & medicinal chemistry letters* **23**, 3039-3043,
1243 doi:10.1016/j.bmcl.2013.03.013 (2013).
1244 38 Davies, T. G. *et al.* Monoacidic Inhibitors of the Kelch-like ECH-Associated Protein 1: Nuclear
1245 Factor Erythroid 2-Related Factor 2 (KEAP1:NRF2) Protein-Protein Interaction with High Cell
1246 Potency Identified by Fragment-Based Discovery. *Journal of medicinal chemistry* **59**,
1247 3991-4006, doi:10.1021/acs.jmedchem.6b00228 (2016).
1248 39 Heightman, T. D. *et al.* Structure-Activity and Structure-Conformation Relationships of Aryl
1249 Propionic Acid Inhibitors of the Kelch-like ECH-Associated Protein 1/Nuclear Factor Erythroid
1250 2-Related Factor 2 (KEAP1/NRF2) Protein-Protein Interaction. *Journal of medicinal chemistry*
1251 **62**, 4683-4702, doi:10.1021/acs.jmedchem.9b00279 (2019).
1252 40 Tran, K. T. *et al.* A Comparative Assessment Study of Known Small-Molecule Keap1-Nrf2
1253 Protein-Protein Interaction Inhibitors: Chemical Synthesis, Binding Properties, and Cellular
1254 Activity. *Journal of medicinal chemistry* **62**, 8028-8052, doi:10.1021/acs.jmedchem.9b00723
1255 (2019).
1256 41 Sivinski, J., Zhang, D. D. & Chapman, E. Targeting NRF2 to treat cancer. *Seminars in cancer*
1257 *biology* **76**, 61-73, doi:10.1016/j.semcancer.2021.06.003 (2021).
1258 42 Abed, D. A., Goldstein, M., Albanyan, H., Jin, H. & Hu, L. Discovery of direct inhibitors of
1259 Keap1-Nrf2 protein-protein interaction as potential therapeutic and preventive agents. *Acta*
1260 *pharmaceutica Sinica. B* **5**, 285-299, doi:10.1016/j.apsb.2015.05.008 (2015).
1261 43 Merritt, J. C. *et al.* Anti-cancer activity of sustained release capsaicin formulations.
1262 *Pharmacology & therapeutics* **238**, 108177, doi:10.1016/j.pharmthera.2022.108177 (2022).
1263 44 Crisman, E. *et al.* KEAP1-NRF2 protein-protein interaction inhibitors: Design, pharmacological
1264 properties and therapeutic potential. *Medicinal research reviews* **43**, 237-287,
1265 doi:10.1002/med.21925 (2023).
1266 45 Luo, X. J., Peng, J. & Li, Y. J. Recent advances in the study on capsaicinoids and capsinoids.
1267 *European journal of pharmacology* **650**, 1-7, doi:10.1016/j.ejphar.2010.09.074 (2011).
1268 46 Peng, J. & Li, Y. J. The vanilloid receptor TRPV1: role in cardiovascular and gastrointestinal
1269 protection. *European journal of pharmacology* **627**, 1-7, doi:10.1016/j.ejphar.2009.10.053
1270 (2010).
1271 47 Baylie, R. L. & Brayden, J. E. TRPV channels and vascular function. *Acta physiologica (Oxford,*
1272 *England)* **203**, 99-116, doi:10.1111/j.1748-1716.2010.02217.x (2011).
1273 48 Begnini, F. *et al.* Importance of Binding Site Hydration and Flexibility Revealed When
1274 Optimizing a Macrocyclic Inhibitor of the Keap1-Nrf2 Protein-Protein Interaction. *Journal of*
1275 *medicinal chemistry* **65**, 3473-3517, doi:10.1021/acs.jmedchem.1c01975 (2022).
1276 49 Guo, Y. *et al.* Network-Based Combinatorial CRISPR-Cas9 Screens Identify Synergistic Modules
1277 in Human Cells. *ACS synthetic biology* **8**, 482-490, doi:10.1021/acssynbio.8b00237 (2019).
1278 50 Zhou, W. *et al.* Network pharmacology to unveil the mechanism of Moluodan in the
1279 treatment of chronic atrophic gastritis. *Phytomedicine : international journal of phytotherapy*
1280 *and phytopharmacology* **95**, 153837, doi:10.1016/j.phymed.2021.153837 (2022).

51 Li, S. Mapping ancient remedies: applying a network approach to traditional Chinese medicine. *Science 350 (6262), S72-S74*.

52 Zhao, S. & Li, S. Network-based relating pharmacological and genomic spaces for drug target identification. *PloS one* **5**, e11764, doi:10.1371/journal.pone.0011764 (2010).

53 Zhang, Y., Chen, L. & Li, S. CIPHER-SC: Disease-Gene Association Inference Using Graph Convolution on a Context-Aware Network With Single-Cell Data. *IEEE/ACM transactions on computational biology and bioinformatics* **19**, 819-829, doi:10.1109/tcbb.2020.3017547 (2022).

54 Lin, X. M. *et al.* Choline Kinase α Mediates Interactions Between the Epidermal Growth Factor Receptor and Mechanistic Target of Rapamycin Complex 2 in Hepatocellular Carcinoma Cells to Promote Drug Resistance and Xenograft Tumor Progression. *Gastroenterology* **152**, 1187-1202, doi:10.1053/j.gastro.2016.12.033 (2017).

55 Zhou, W. *et al.* Network pharmacology to explore the anti-inflammatory mechanism of Xuebijing in the treatment of sepsis. *Phytomedicine : international journal of phytotherapy and phytopharmacology* **85**, 153543, doi:10.1016/j.phymed.2021.153543 (2021).

56 Xu, H. *et al.* Bioactive compounds from Huashi Baidu decoction possess both antiviral and anti-inflammatory effects against COVID-19. *Proceedings of the National Academy of Sciences of the United States of America* **120**, e2301775120, doi:10.1073/pnas.2301775120 (2023).

57 Zhang, X. J. *et al.* Proteome profiling of spinal cord and dorsal root ganglia in rats with trinitrobenzene sulfonic acid-induced colitis. *World journal of gastroenterology* **18**, 2914-2928, doi:10.3748/wjg.v18.i23.2914 (2012).

58 张彦琼，李梢. 网络药理学与中医药现代研究的若干进展. *中国药理学与毒理学杂志* **29 (6),883-892** (2015).

59 Sun, Y. *et al.* Andrographolide protects bone marrow mesenchymal stem cells against glucose and serum deprivation under hypoxia via the NRF2 signaling pathway. *Stem cell research & therapy* **13**, 326, doi:10.1186/s13287-022-03016-6 (2022).

60 Meiler, J. & Baker, D. ROSETTALIGAND: protein-small molecule docking with full side-chain flexibility. *Proteins* **65**, 538-548, doi:10.1002/prot.21086 (2006).

61 Van Der Spoel, D. *et al.* GROMACS: fast, flexible, and free. *Journal of computational chemistry* **26**, 1701-1718, doi:10.1002/jcc.20291 (2005).

62 Kim, S. *et al.* CHARMM-GUI ligand reader and modeler for CHARMM force field generation of small molecules. *Journal of computational chemistry* **38**, 1879-1886, doi:10.1002/jcc.24829 (2017).

Figure legends

Figure 1. Capsaicin reduces ROS and promotes NRF2 expression. (a) Microscopic examination of GES-1 cellular morphology following treatment regimens. Cells were pre-treated with Capsaicin (CAP) at concentrations of 2 or 8 μM for 2.5 hours, followed by incubation with 5% EtOH for 1.5 hours. Scale bar, 50 μm. **(b)** Detection of ROS-positive GES-1 cells using DCFH-DA

staining. Scale bar, 200 μm. **(c)** Flow cytometric (FCM) analysis of ROS-positive GES-1 cells labeled with DCFH-DA. **(d)** Statistical analysis of ROS levels measured by FCM. The experiment was conducted in triplicate. **(e)** Assessment of SOD activity in GES-1 cells. **(f)** Quantification of MDA levels of GES-1 cells. **(g)** A network targets of CAP. Purple, blue, pink nodes represent proteins or genes in the predicted biological effect profile of CAP related to ROS, inflammation or immune, respectively. **(h)** Heatmap depicting differentially expressed genes (DEGs) enriched in antioxidant activity based on proteomic analysis. Each row represents the expression level of a single gene, while each column corresponds to an individual experimental sample. **(i)** Western blot analysis of NRF2 and HO-1 expression in GES-1 cells. **(j)** Western blot assessment of antioxidant protein expression in GES-1 cells. **(k)** Quantitative analysis of relative mRNA levels of antioxidant response elements (ARE)-related genes in GES-1 cells. Cells were treated with or without CAP and EtOH, and the mRNA levels of TXN, HMOX1, and NQO1 were measured. Each group consisted of three replicates. **(l)** Western blot analysis of NRF2 and HO-1 expression in human umbilical cord mesenchymal stem cells (HUC-MSCs). **(m)** Quantitative analysis of relative mRNA levels of ARE-related genes in HUC-MSCs. The mRNA levels of TXN, HMOX1, and NQO1 were measured in different treatment groups. Data were presented as mean ± SD. P-values were calculated using a T-test. Significance levels were indicated as follows: ns, not significant; *$p < 0.05$; **$p < 0.01$; ***$p < 0.001$; ****$p < 0.0001$.

Figure 2. Capsaicin inhibits the ubiquitination and degradation of NRF2. **(a)** Immunofluorescence detection of NRF2 nuclear localization DAPI was employed to label the cell nuclei for reference. Scale bar, 100 μm. **(b)** Statistical analysis of NRF2 nuclear translocation following 8 μM CAP pre-treatment. The proportion of NRF2 localized in the nucleus post-CAP treatment was quantitatively assessed. **(c and d)** Subcellular localization of

NRF2 in GES-1 cells across different treatment groups. NRF2 levels in both the nucleus and cytoplasm were assessed. GAPDH was used as a cytoplasmic marker, and Histone H3 served as a nuclear marker. Statistical analysis was performed specifically on the nuclear localization of Nrf2. **(e)** Total NRF2 levels induced by PS-341 or CAP. **(f)** Analysis of total NRF2 levels under the influence of cycloheximide (CHX), With or Without 8 μM CAP treatment. NRF2 degradation was semi-quantitatively assessed using ImageJ software to analyze the western blot results. **(g-h)** Inhibition of K48 ubiquitination on NRF2 protein by 8 μM CAP as assessed by Co-IP assay in 293T cells. **(i)** Mitochondrial visualization in GES-1 cells following CAP and EtOH treatment regimens. Cells were pre-treated with CAP at concentrations of 2 or 8 μM for 2.5 hours, followed by a 10-minute incubation with 5% EtOH. Mitochondria were labeled with Mito Tracker Red CMXRos and detected via immunofluorescence. Red fluorescence indicates the mitochondria, while blue fluorescence (DAPI staining) marks the cell nucleus. Scale bar represents 100 μm. **(j)** Quantitative analysis of mitochondrial branch length in different treatment groups using ImageJ and GraphPad Prism. The branch length of individual mitochondria was analyzed using ImageJ software and the data were plotted using GraphPad Prism. **(k)** Assessment of mitochondrial membrane potential (ΔΨm) in GES-1 cells using FCM. Cells were pre-treated with CAP at concentrations of 2 or 8 μM for 2.5 hours, followed by a 10-minute incubation with 5% EtOH or a 20-minute incubation with CCCP as a positive control. ΔΨm was evaluated using JC-10 staining. **(l)** Quantitative analysis of ΔΨm across different treatment groups using ImageJ Software. Data were presented as mean ± SD. P-values were calculated using a T-test. Significance levels were indicated as follows: ns, not significant; *$p < 0.05$; **$p < 0.01$; ***$p < 0.001$; ****$p < 0.0001$.

Figure 3. Capsaicin disrupted KEAP1-NRF2 interaction. (a-b) Assessment of KEAP1 transcription and expression levels using RT-qPCR and western blot

analyses. **(c)** KEAP1-NRF2 interaction was detected with Surface plasmon resonance (SPR) in *vitro*. **(d)** Disruption of KEAP1-NRF2 interaction by CAP as assessed by SPR. **(e)** Disruption of KEAP1-NRF2 interaction by 32 μM CAP as assessed by Co-Immunoprecipitation (Co-IP) in 293T Cells. **(f)** Quantitative analysis of relative NRF2 expression in IP samples using ImageJ software. **(g)** Cell viability assessment of 293T cells treated with CAP and EtOH using CCK-8 assay. **(h)** Western blot analysis of NRF2 and HO-1 expression in 293T cells. **(i)** Cell viability assessment of 293T(KO) cells treated with CAP and EtOH using CCK-8 assay. **(j)** Western blot analysis of NRF2 and HO-1 expression in 293T(KO) cells. Data were presented as mean ± SD. P-values were calculated using a T-test. Significance levels were indicated as follows: ns, not significant; *$p < 0.05$; **$p < 0.01$; ***$p < 0.001$; ****$p < 0.0001$.

Figure 4. CAP specifically interacts with the Kelch domain of KEAP1. (a) Detection of KEAP1-CAP interaction in GES-1 cells using cellular thermal shift assay coupled with western blotting (CETSA-WB) and the melting curve generated from CETSA was analyzed using ImageJ software. The red fold line represents cells treated with CAP, while the black fold line represents cells treated with DMSO as a control. **(b)** Computational docking of CAP molecule to KEAP1 surface pockets. The Keap1 protein is represented in gray, while the CAP molecule is shown in yellow. The seven key amino acids predicted to be crucial for the interaction are highlighted in blue. **(c)** Partial overlap of CAP-binding pocket with KEAP1-NRF2 interface. The KEAP1-NRF2 interaction interface is represented in purple. **(d)** Influence of dithiothreitol (DTT) on NRF2 activation induced by CAP in GES-1 cells. Cells were pre-incubated with 400 μM DTT for 1 hour, followed by a 3-hour incubation with 32 μM CAP. **(e)** Tandem mass spectrometry (MS/MS) of analysis of KEAP1 peptide containing Cys151 following CAP treatment. **(f)** Dose-dependent examination of Kelch-NRF2 interaction in the presence of CAP in 293T cells. Cells were treated with varying concentrations of CAP (0, 62.5, 125, 250, and

500 μM) to assess the impact on the interaction between exogenously purified Kelch protein and NRF2 in the total cell lysate. **(g)** Pull-Down assay demonstrating the direct inhibition of Kelch-NRF2 Interaction by CAP. Data were presented as mean ± SD. P-values were calculated using a T-test. Significance levels were indicated as follows: ns, not significant; *p < 0.05; **p < 0.01; ***p < 0.001; ****p < 0.0001.

Figure 5. Mutation of KEAP1 affects the action of CAP. (a) *In vitro* detection of KEAP1-Kelch domain with CAP using BLI. **(b)** *In vitro* detection of KEAP1-Kelch domain (Mut) with CAP using BLI. **(c)** Co-IP assay to assess the interaction between mutant Kelch and NRF2, and the Impact of 32 μM CAP on Kelch-NRF2 binding in 293T cells. **(d)** Docking analysis reveals encirclement of CAP's vanillyl headgroup by main chain atoms of the Kelch domain. **(e)** Left side.：existing binding sites of two common ligands with Kelch (PDB:4IQK and 5FNQ); Right side：newly discovered binding sites of CAP with Kelch. Data were presented as mean ± SD. P-values were calculated using a T-test. Significance levels were indicated as follows: ns, not significant; *p < 0.05; **p < 0.01; ***p < 0.001; ****p < 0.0001.

Figure 6 Preparation and characterization of IR-HSA@CAP NPs. (a) Schematic illustration of the synthesis process for IR-HSA@CAP nanoparticles (NPs). **(b)** Determination of IRDye800 binding with HSA by UV-Vis spectra. **(c)** The morphology of IR-HSA@CAP NPs was investigated by transmission electron microscope. Scale bar, 0.5 μm. **(d-e)** Particle size comparison of HSA@CAP and IR-HSA@CAP NPs. **(f)** Zeta-Potential analysis of nanomaterials. The zeta-potential values of the different materials were measured: H representing HSA, HC representing HSA@CAP NPs, and IHC representing IR-HSA@CAP NPs. **(g)** FCM analysis demonstrates endocytosis of IR-HSA@CAP NPs by GES-1 cells. **(h-i)** Detection of CAP release in

simulated gastric fluid (SGF) and stroke-physiological saline solution (SPSS) Using high-performance liquid chromatography (HPLC). **(j)** *In vivo* imaging reveals the localization of IR-HSA@CAP NPs. **(k)** Observing the distribution of IR-HSA@CAP NPs in major organs of rats. Data were presented as mean ± SD. P-values were calculated using a T-test. Significance levels were indicated as follows: ns, not significant; *p < 0.05; **p < 0.01; ***p < 0.001; ****p < 0.0001.

Figure 7 CAP activated NRF2/ARE pathway *in vivo*. (a) Impact of CAP (1 mg/kg) on histopathology of EtOH-induced gastric mucosal injury. Rebamipide (100 mg/kg) was used as a positive control. Tissue sections were stained and evaluated for gastric mucosal ulcer injury using the Guth scoring system. Representative images were shown with a scale bar of 5 mm. The ulcer injury (UI) index was calculated. **(b)** Histological examination of rat gastric mucosa using H&E staining. Scale bar represents 400 μm. A: Inflammatory cell infiltration; B: Epithelial exfoliation; C: Glandular disorder; D: Gastric edema. Quantitative analysis was conducted using the Masuda scoring system. **(c)** Visualization of ROS in rat gastric tissue under various treatments using DHE staining and inverted fluorescence microscopy. Scale bar represents 50 μm. ROS levels were quantified using Image Pro Plus 6.0 software. **(d)** MDA levels in gastric tissues across different treatment groups. **(e)** Assessment of catalase (CAT) activity in gastric tissues. **(f)** Measurement of HMOX1 and NQO1 mRNA levels in gastric tissues using RT-qPCR. Data were presented as mean ± SD. Significance levels were indicated as follows: ns, not significant; *p < 0.05; **p < 0.01; ***p < 0.001; ****p < 0.0001 compared to the EtOH-only group (marked in blue).

Figure 8 CAP also suppressed inflammation *in vivo*. (a-c) Immunohistochemical detection of antioxidant proteins and presentation of representative images and statistical analysis results. (a) Nrf2, (b) HO-1, and

(c) Trx protein expression levels were assessed. **(d)** ELISA measurement of IL-1β, TNF-α, IL-6, CXCL1/KC (IL-8), and IL-10 Levels in gastric tissues. Data were presented as mean ± SD. Significance levels were indicated as follows: ns, not significant; *$p < 0.05$; **$p < 0.01$; ***$p < 0.001$; ****$p < 0.0001$ compared to the EtOH-only group (marked in blue). **(e)** Mechanism diagram of capsaicin alleviating gastric mucosal injury caused by ethanol in rats.

Graphic diagram

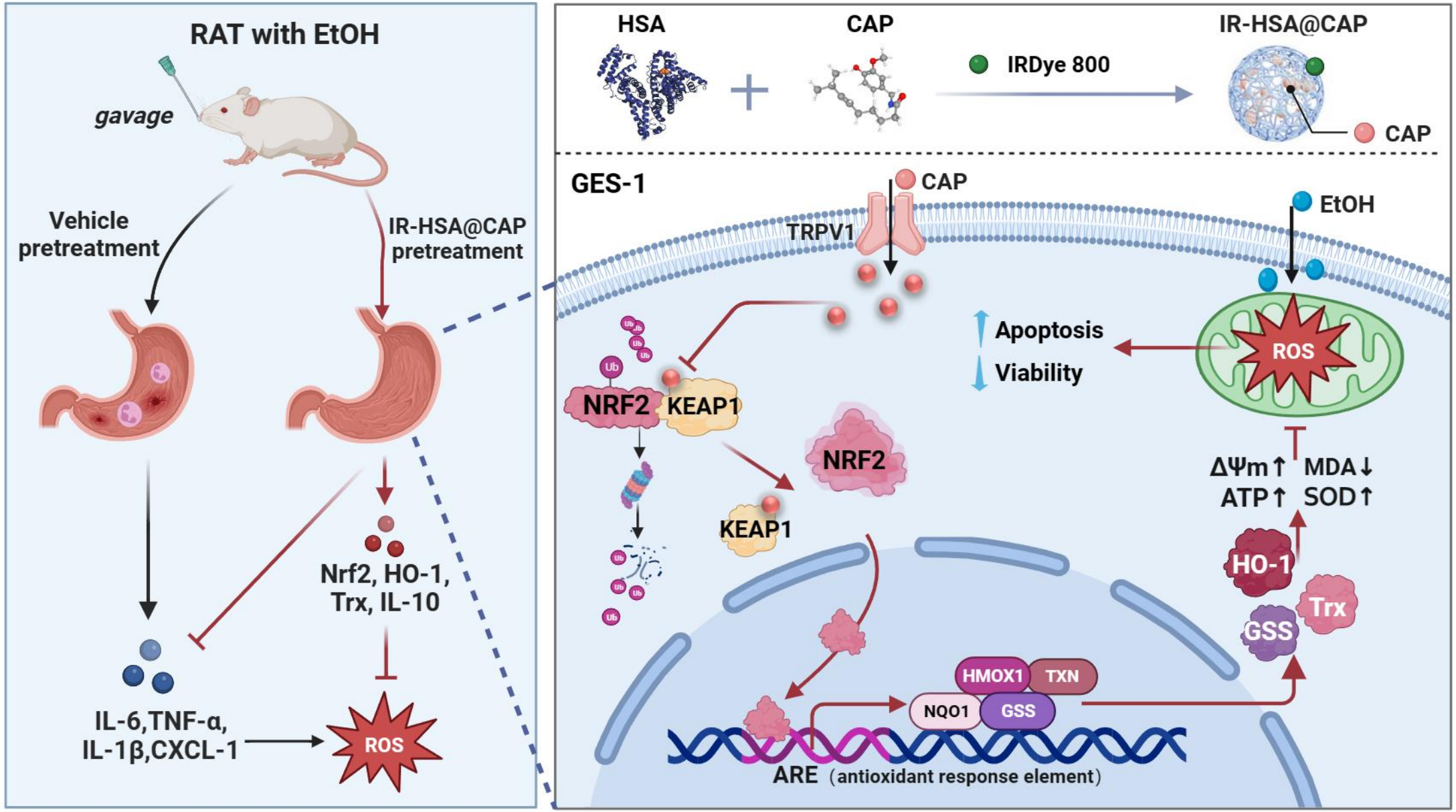

Figure 1

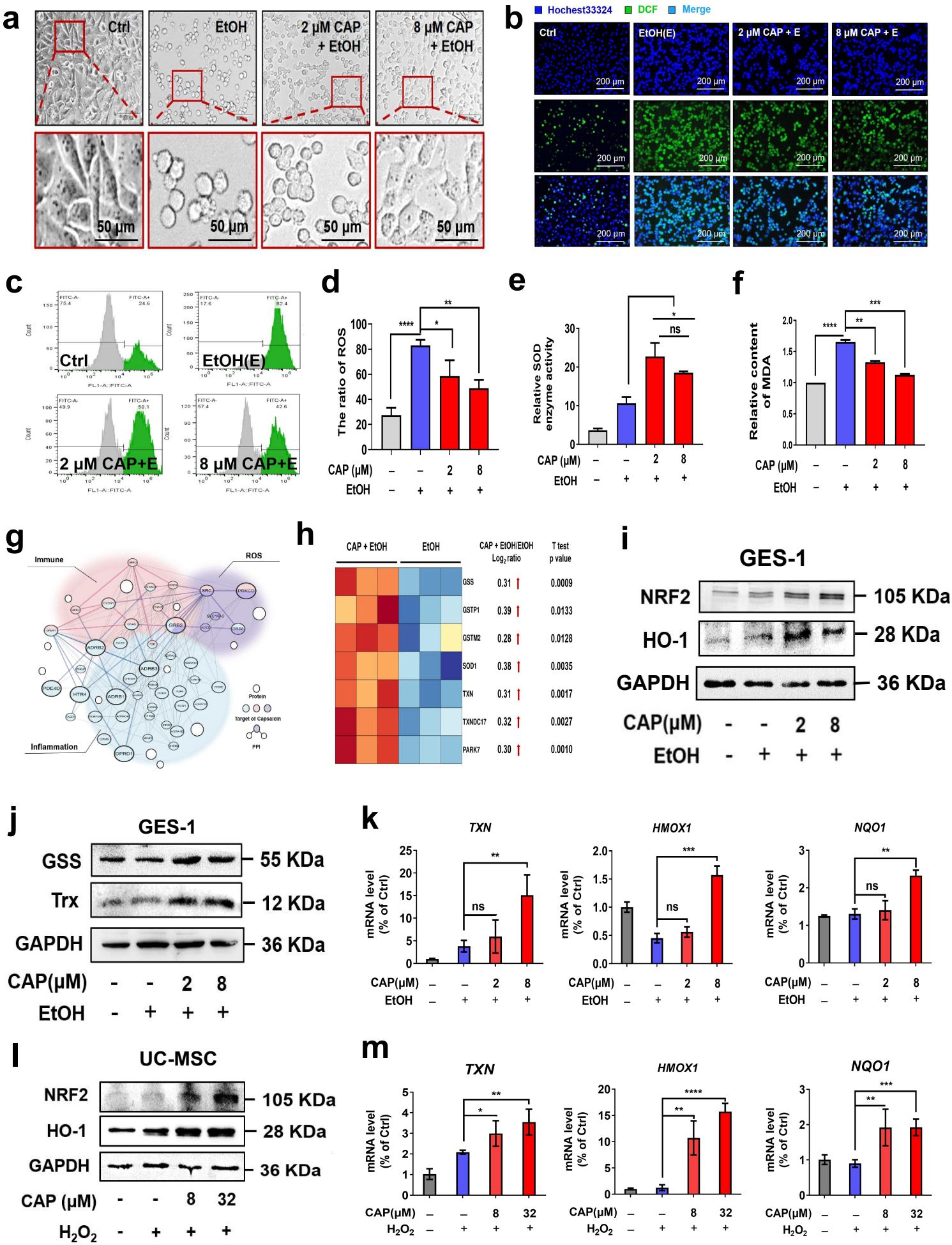
a
Ctrl
EtOH
2 μM CAP + EtOH
8 μM CAP + EtOH
50 μm
b
Hochest33324
DCF
Merge
Ctrl
EtOH(E)
2 μM CAP + E
8 μM CAP + E
200 μm
c
Ctrl
EtOH(E)
2 μM CAP+E
8 μM CAP+E
d
The ratio of ROS
CAP (μM)
EtOH
e
Relative SOD enzyme activity
f
Relative content of MDA
g
Immune
ROS
Inflammation
Protein
Target of Capsaicin
PPI
h
CAP + EtOH
EtOH
CAP + EtOH/EtOH Log2 ratio
T test p value
GSS 0.31 0.0009
GSTP1 0.39 0.0133
GSTM2 0.28 0.0128
SOD1 0.38 0.0035
TXN 0.31 0.0017
TXNDC17 0.32 0.0027
PARK7 0.30 0.0010
i
GES-1
NRF2 105 KDa
HO-1 28 KDa
GAPDH 36 KDa
CAP(μM) - - 2 8
EtOH - + + +
j
GES-1
GSS 55 KDa
Trx 12 KDa
GAPDH 36 KDa
CAP(μM) - - 2 8
EtOH - + + +
k
TXN
HMOX1
NQO1
mRNA level (% of Ctrl)
CAP(μM)
EtOH
l
UC-MSC
NRF2 105 KDa
HO-1 28 KDa
GAPDH 36 KDa
CAP (μM) - - 8 32
H2O2 - + + +
m
TXN
HMOX1
NQO1
mRNA level (% of Ctrl)
CAP(μM)
H2O2

Figure 2

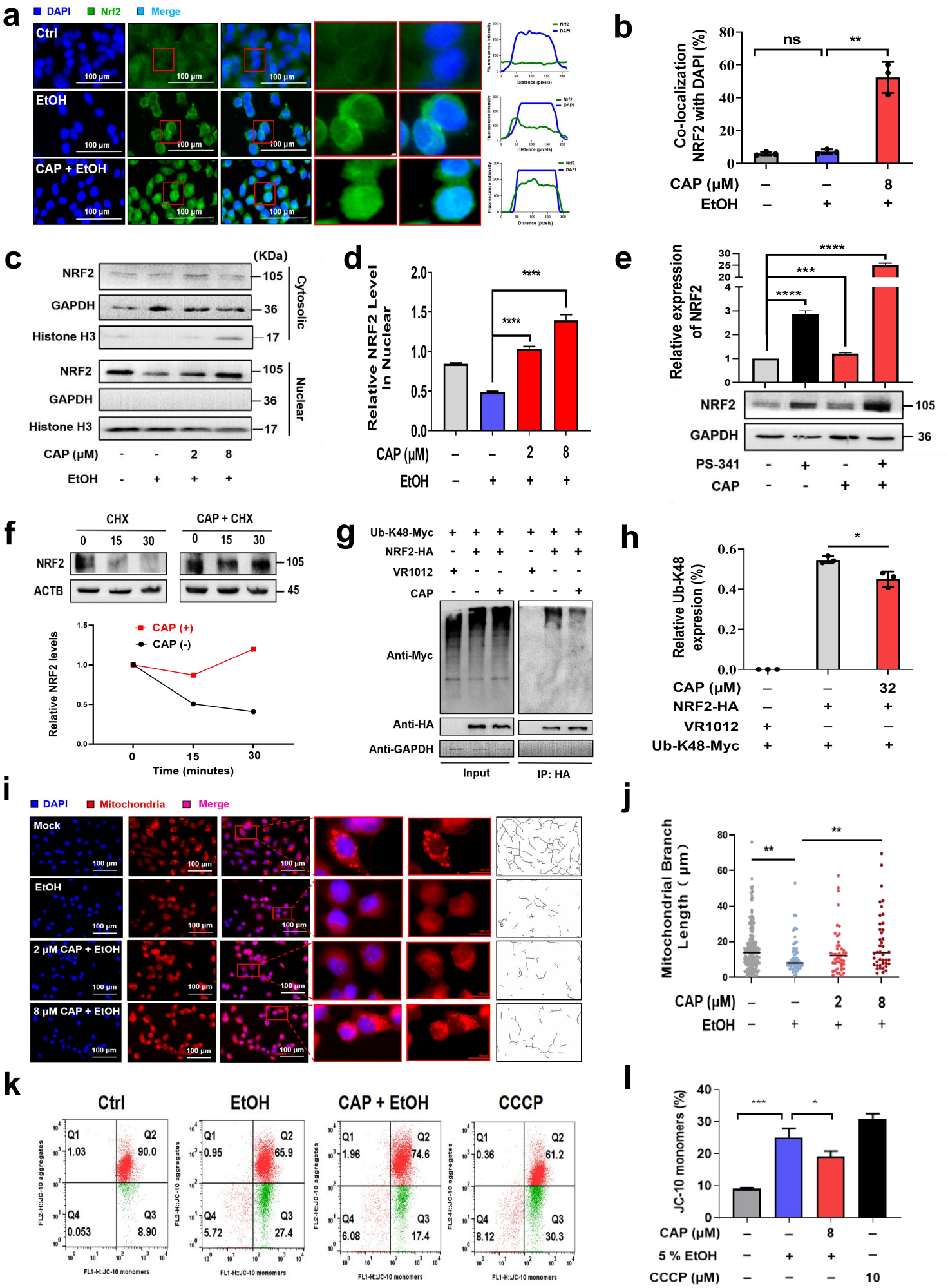
a
DAPI
Nrf2
Merge
Ctrl
EtOH
CAP + EtOH
100 μm
b
Co-localization NRF2 with DAPI (%)
ns
**
CAP (μM) – – 8
EtOH – + +
c
(KDa)
NRF2
GAPDH
Histone H3
105
36
17
Cytosolic
Nuclear
CAP (μM) - - 2 8
EtOH - + + +
d
Relative NRF2 Level In Nuclear
****
CAP (μM) – – 2 8
EtOH – + + +
e
Relative expression of NRF2
***
PS-341 - + - +
CAP - - + +
f
CHX
CAP + CHX
0 15 30
ACTB
45
CAP (+)
CAP (-)
Relative NRF2 levels
Time (minutes)
g
Ub-K48-Myc
NRF2-HA
VR1012
CAP
Anti-Myc
Anti-HA
Anti-GAPDH
Input
IP: HA
h
Relative Ub-K48 expresion (%)
*
CAP (μM) – – 32
NRF2-HA – + +
VR1012 + – –
Ub-K48-Myc + + +
i
Mitochondria
Merge
Mock
2 μM CAP + EtOH
8 μM CAP + EtOH
j
Mitochondrial Branch Length（μm）
CAP (μM) – – 2 8
EtOH – + + +
k
Ctrl
EtOH
CAP + EtOH
CCCP
Q1 1.03 Q2 90.0 Q4 0.053 Q3 8.90
Q1 0.95 Q2 65.9 Q4 5.72 Q3 27.4
Q1 1.96 Q2 74.6 Q4 6.08 Q3 17.4
Q1 0.36 Q2 61.2 Q4 8.12 Q3 30.3
FL2-H::JC-10 aggregates
FL1-H::JC-10 monomers
l
JC-10 monomers (%)
CAP (μM) – – 8 –
5 % EtOH – + + –
CCCP (μM) – – – 10

Figure 3

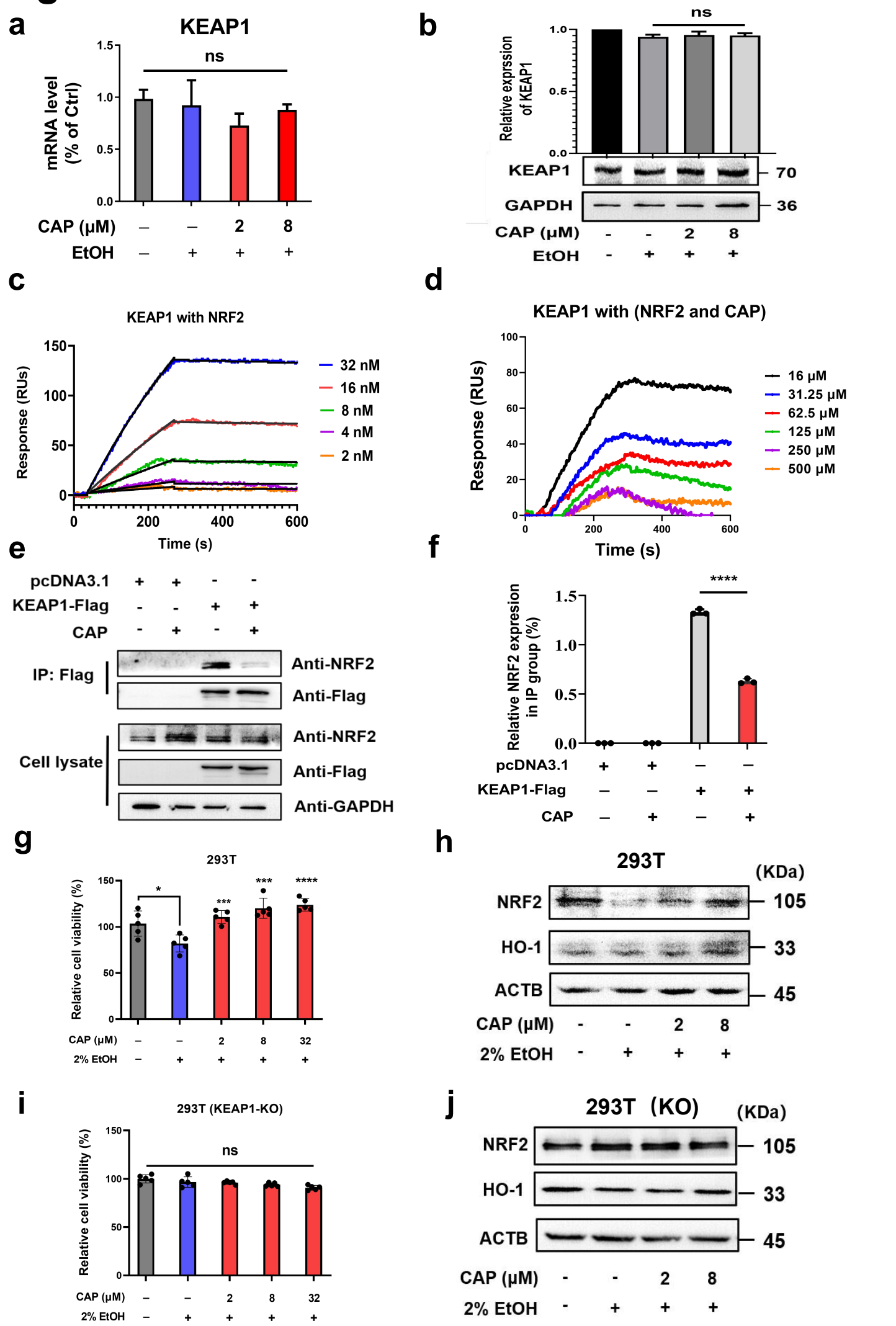
a
KEAP1
ns
mRNA level (% of Ctrl)
1.5
1.0
0.5
0.0
CAP (μM) – – 2 8
EtOH – + + +
b
ns
Relative exprssion of KEAP1
1.0
0.5
0.0
KEAP1
70
GAPDH
36
CAP (μM) - - 2 8
EtOH - + + +
c
KEAP1 with NRF2
Response (RUs)
150
100
50
0
0 200 400 600
Time (s)
32 nM
16 nM
8 nM
4 nM
2 nM
d
KEAP1 with (NRF2 and CAP)
Response (RUs)
100
80
60
40
20
0
0 200 400 600
Time (s)
16 μM
31.25 μM
62.5 μM
125 μM
250 μM
500 μM
e
pcDNA3.1 + + - -
KEAP1-Flag - - + +
CAP - + - +
IP: Flag
Anti-NRF2
Anti-Flag
Cell lysate
Anti-NRF2
Anti-Flag
Anti-GAPDH
f
****
Relative NRF2 expresion in IP group (%)
1.5
1.0
0.5
0.0
pcDNA3.1 + + – –
KEAP1-Flag – – + +
CAP – + – +
g
293T
Relative cell viability (%)
150
100
50
0
*
***
***
****
CAP (μM) – – 2 8 32
2% EtOH – + + + +
h
293T
(KDa)
NRF2
105
HO-1
33
ACTB
45
CAP (μM) - - 2 8
2% EtOH - + + +
i
293T (KEAP1-KO)
Relative cell viability (%)
150
100
50
0
ns
CAP (μM) – – 2 8 32
2% EtOH – + + + +
j
293T (KO)
(KDa)
NRF2
105
HO-1
33
ACTB
45
CAP (μM) - - 2 8
2% EtOH - + + +

Figure 4

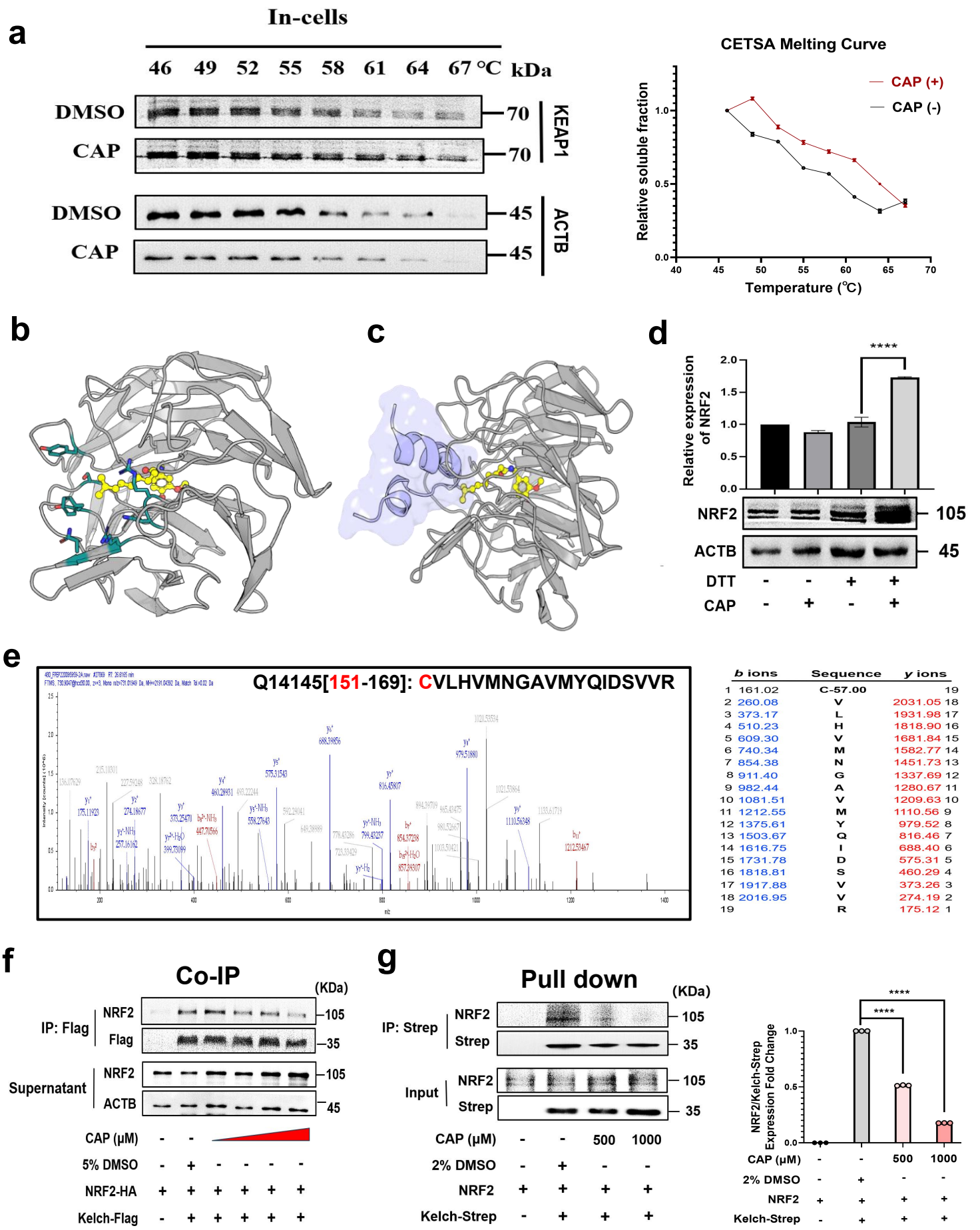
a
In-cells
46 49 52 55 58 61 64 67 °C kDa
DMSO
CAP
70
70
KEAP1
DMSO
CAP
45
45
ACTB
CETSA Melting Curve
CAP (+)
CAP (-)
Relative soluble fraction
Temperature (°C)
b
c
d
Relative expression of NRF2
****
NRF2
ACTB
105
45
DTT - - + +
CAP - + - +
e
Q14145[151-169]: CVLHVMNGAVMYQIDSVVR
b ions Sequence y ions
1 161.02 C-57.00 19
2 260.08 V 2031.05 18
3 373.17 L 1931.98 17
4 510.23 H 1818.90 16
5 609.30 V 1681.84 15
6 740.34 M 1582.77 14
7 854.38 N 1451.73 13
8 911.40 G 1337.69 12
9 982.44 A 1280.67 11
10 1081.51 V 1209.63 10
11 1212.55 M 1110.56 9
12 1375.61 Y 979.52 8
13 1503.67 Q 816.46 7
14 1616.75 I 688.40 6
15 1731.78 D 575.31 5
16 1818.81 S 460.29 4
17 1917.88 V 373.26 3
18 2016.95 V 274.19 2
19 R 175.12 1
f
Co-IP
(KDa)
IP: Flag
NRF2
Flag
105
35
Supernatant
NRF2
ACTB
105
45
CAP (μM) - -
5% DMSO - + - - - -
NRF2-HA + + + + + +
Kelch-Flag - + + + + +
g
Pull down
(KDa)
IP: Strep
NRF2
Strep
105
35
Input
NRF2
Strep
105
35
CAP (μM) - - 500 1000
2% DMSO - + - -
NRF2 + + + +
Kelch-Strep - + + +
NRF2/Kelch-Strep Expression Fold Change
****
****
CAP (μM) - - 500 1000
2% DMSO - + - -
NRF2 + + + +
Kelch-Strep - + + +

Figure 5

a KEAP1-Kelch domain

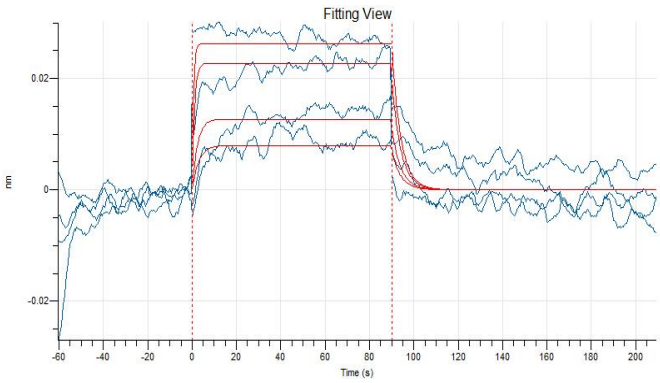

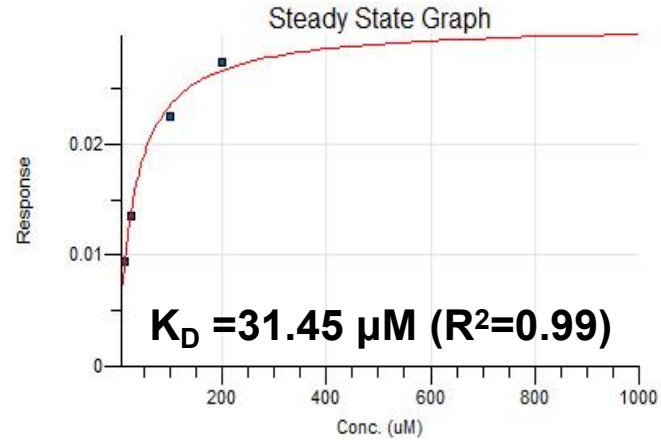

b KEAP1-Kelch domain (Mut)

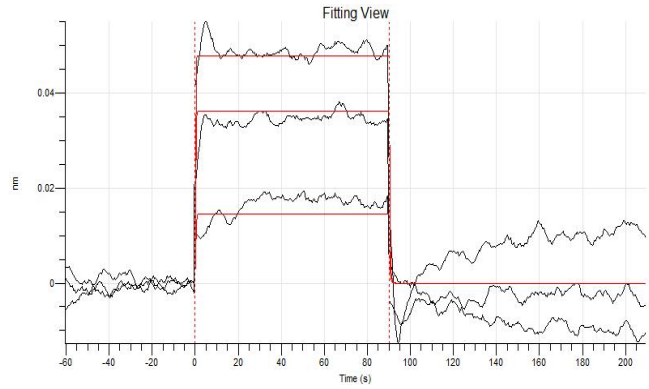

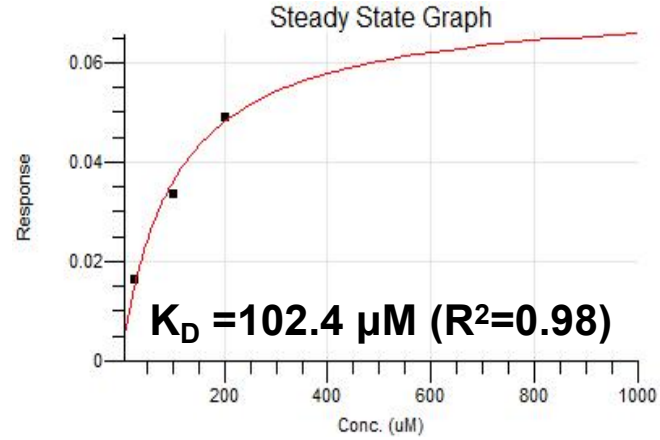

c

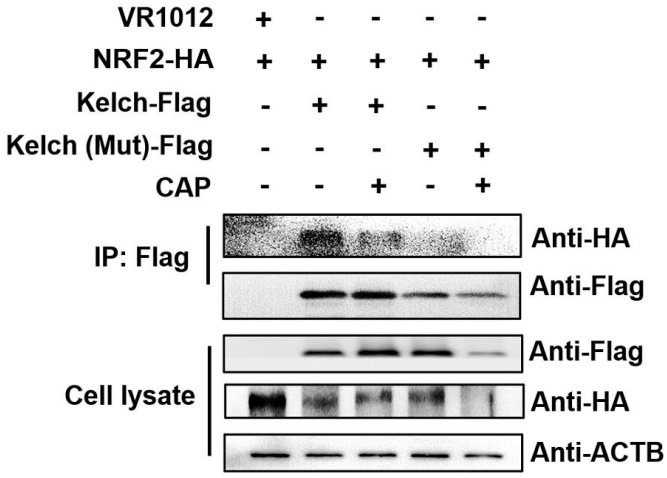

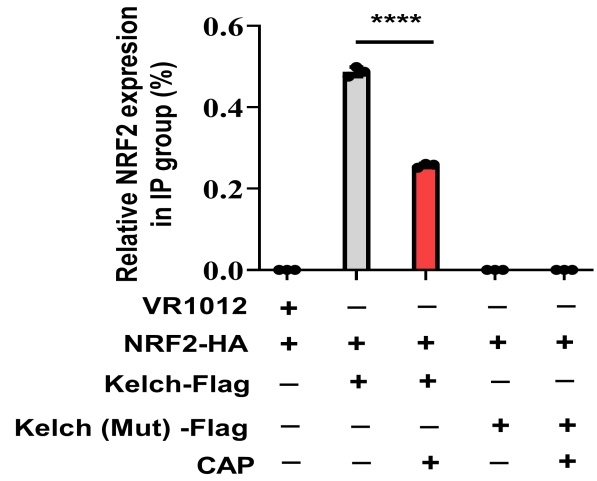

d

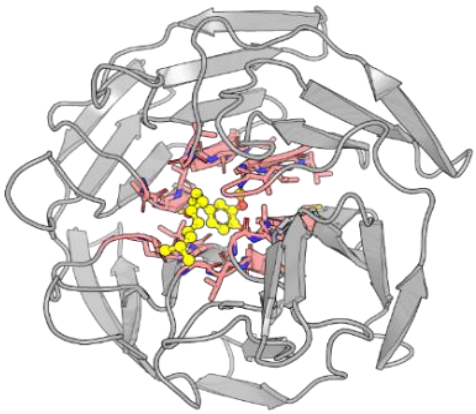

e PDB: 4IQK;5FNQ

CAP

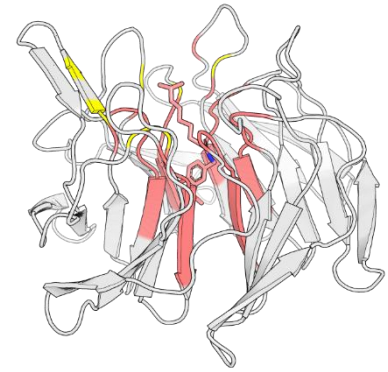

Figure 6

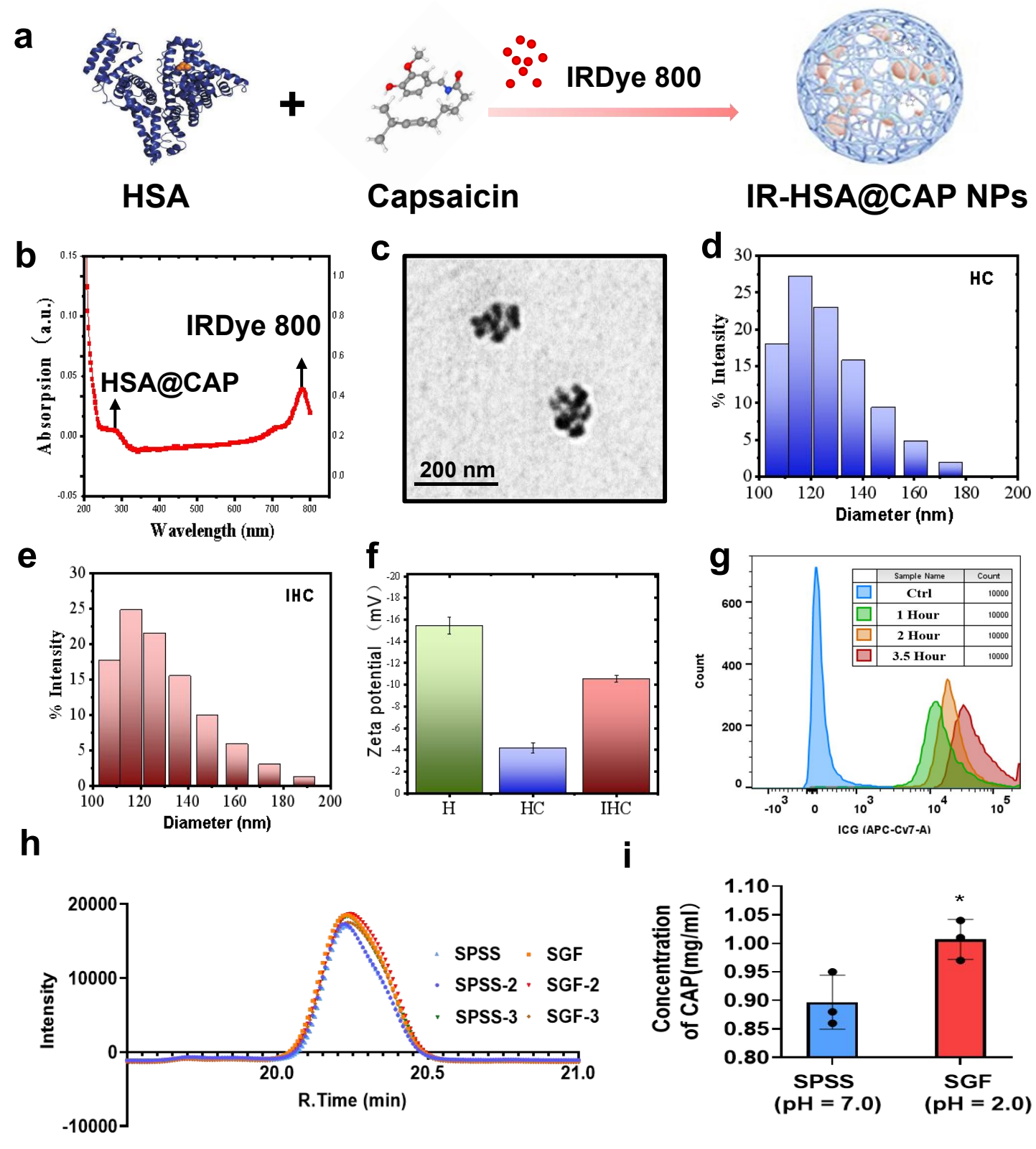
a
HSA
Capsaicin
IRDye 800
IR-HSA@CAP NPs
b
IRDye 800
HSA@CAP
Absorpsion (a.u.)
Wavelength (nm)
c
200 nm
d
HC
% Intensity
Diameter (nm)
e
IHC
% Intensity
Diameter (nm)
f
Zeta potential (mV)
H
HC
IHC
g
Sample Name
Count
Ctrl
1 Hour
2 Hour
3.5 Hour
Count
ICG (APC-Cy7-A)
h
Intensity
R.Time (min)
SPSS
SPSS-2
SPSS-3
SGF
SGF-2
SGF-3
i
Concentration of CAP(mg/ml)
SPSS (pH = 7.0)
SGF (pH = 2.0)
j
10 min
20 min
30 min
45 min
60 min
45 min (Side)
k
He
Li
Sp
Lu
Ki
St
Lg
Je
Du
45 min
60 min

Figure 7

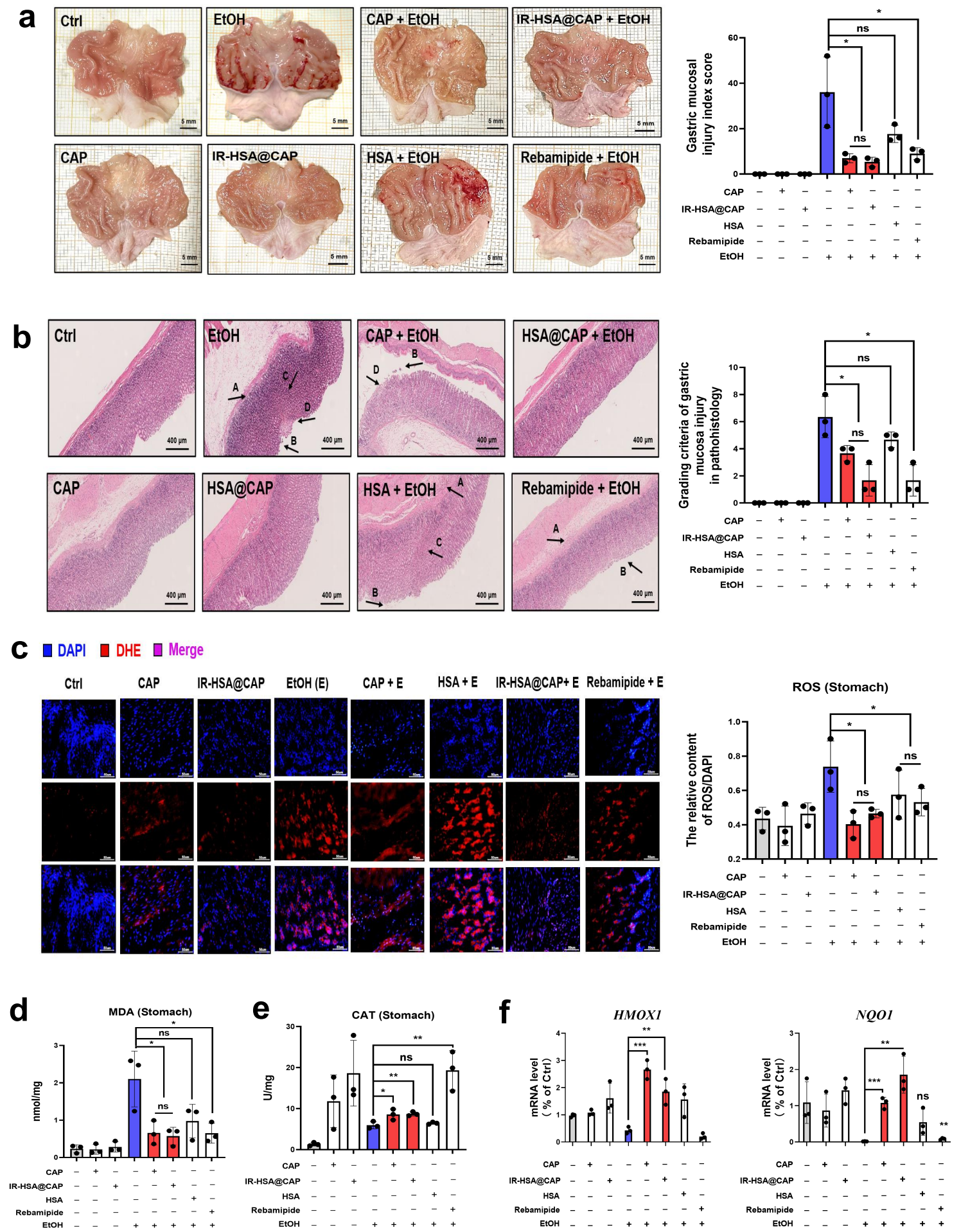
a
Ctrl
EtOH
CAP + EtOH
IR-HSA@CAP + EtOH
CAP
IR-HSA@CAP
HSA + EtOH
Rebamipide + EtOH
5 mm
Gastric mucosal injury index score
CAP
IR-HSA@CAP
HSA
Rebamipide
EtOH
b
Ctrl
EtOH
CAP + EtOH
HSA@CAP + EtOH
CAP
HSA@CAP
HSA + EtOH
Rebamipide + EtOH
400 μm
Grading criteria of gastric mucosa injury in pathohistology
c
DAPI
DHE
Merge
Ctrl
CAP
IR-HSA@CAP
EtOH (E)
CAP + E
HSA + E
IR-HSA@CAP+ E
Rebamipide + E
ROS (Stomach)
The relative content of ROS/DAPI
d
MDA (Stomach)
nmol/mg
e
CAT (Stomach)
U/mg
f
HMOX1
NQO1
mRNA level (% of Ctrl)

Figure 8

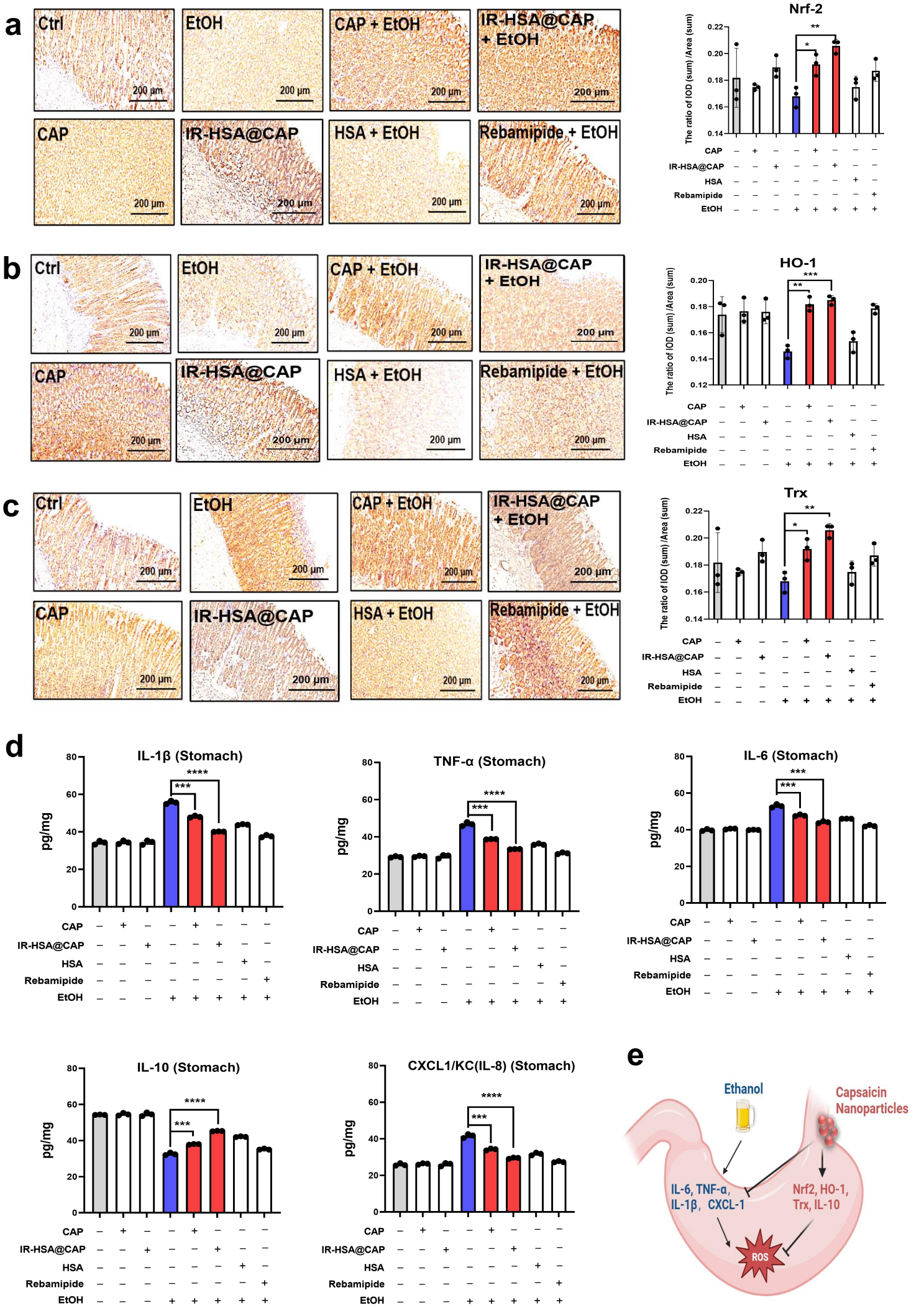
a
Ctrl
EtOH
CAP + EtOH
IR-HSA@CAP + EtOH
CAP
IR-HSA@CAP
HSA + EtOH
Rebamipide + EtOH
200 μm
Nrf-2
The ratio of IOD (sum) /Area (sum)
CAP
IR-HSA@CAP
HSA
Rebamipide
EtOH
b
HO-1
c
Trx
d
IL-1β (Stomach)
TNF-α (Stomach)
IL-6 (Stomach)
IL-10 (Stomach)
CXCL1/KC(IL-8) (Stomach)
pg/mg
e
Ethanol
Capsaicin Nanoparticles
IL-6, TNF-α, IL-1β, CXCL-1
Nrf2, HO-1, Trx, IL-10
ROS

Supplementary Materials for

Capsaicin acts as a novel NRF2 agonist to suppress oxidative stress by directly disrupting the KEAP1-NRF2 interaction

Xiaoning Gao[1, †], Bo Zhang[2, †], Peiyuan Liu[1, †], Mingyue Yuwen[1], Zixiang Liu[1], Ruyang Tan[1], Boyang Wang[2], Kairui Liu[1], Zhiru Yang[1], Junli Ba[1], Xue Bai[1], Shiti Shama [1], Cong Tang[1], Cheng Zhu[1, *], Tao Wang[1, *], Shao Li[2,3, *], Jun Kang[1, *]

[1] School of Life Sciences, Tianjin University, 92 Weijin Road, Nankai District, Tianjin 300072, People's Republic of China

[2] Institute for TCM-X, MOE Key Laboratory of Bioinformatics, Bioinformatics Division, BNRist, Department of Automation, Tsinghua University, No. 30 Shuangqing Road, Haidian District, Beijing 100084, People's Republic of China.

[3] Department of Molecular Pharmacology, Tianjin Medical University Cancer Institute & Hospital; National Clinical Research Center for Cancer; Key Laboratory of Cancer Prevention and Therapy, Tianjin; Tianjin's Clinical Research Center for Cancer, Tianjin 300060, China.

* Correspondence:

Jun Kang, jun.kang@tju.edu.cn; Shao Li, shaoli@mail.tsinghua.edu.cn；

Tao Wang，wangtaobio@tju.edu.cn; Cheng Zhu，cheng_zhu@tju.edu.cn

† These authors contributed equally to this work.

This PDF file includes:

Figures. S1 to S7

Videos. S1 and S2 (MP4)

SUPPLYMENTARY FIGURE LEGEND

Fig. S1 Capsaicin protects GES-1 from oxidative stress

(a) Molecular formula of CAP from PubChem (Compound CID: 1548943). **(b)** Cell viability of GES-1 after 1.5 h treatment with ethanol at different concentrations (v/v). Data were presented as mean ± SD, P values were calculated using T-test. *p< 0.05. **p< 0.01. **(c)** Cell viability of GES-1 after pretreatment with different concentrations of CAP for 2.5 h and adding 5% ethanol for 1.5 h. Data were presented as mean ± SD, P values were calculated using T-test. ns, not significant; **p< 0.01. **(d)** Effects of different concentrations of CAP on the viability of GES-1 cells for 24 h. Data were presented as mean ± SD, P values were calculated using T-test (Compared with the Ctrl). ns, not significant; ****p< 0.0001. **(e-g)** Cell viability was measured by adding CAP (2 μM, 8 μM or 32 μM) to GES-1 cells for 2.5 hours and then adding three concentrations of ethanol (0.5%, 3.5% and 5%) for another 1.5 hours. ns, not significant; *p< 0.05.**p< 0.01. **(h)** FCM showed CAP inhibited the apoptosis of GES-1 induced by EtOH.

Fig. S2 Potential pathways and proteins that CAP may affect.

(a) Heat map showed the up-regulation and down-regulation of all differentially expressed proteins in CAP (8 μM, 2.5 h) and 5% EtOH (1.5 h) versus 5%EtOH (1.5 h) alone. Red and blue are indicative of increased and decreased expression, respectively. **(b)** GO enrichment analysis of differentially expressed genes (DEGs). **(c)** KEGG enrichment analysis of DEGs. **(d)** Volcano plot illustrating DEGs between two treatment groups in GES-1 cells. Genes with significantly increased expression were marked in red, while those with significantly decreased expression were marked in blue. **(e-h)** Grayscale analysis of WB in GES-1. Statistical results of the expression of total Nrf2, HO-1, GSS and Trx compared with internal reference protein GAPDH. Experiments were repeated 3 times. Data were presented as mean ± SD, P values were calculated using T-test. ns, not significant; ****p< 0.0001. **(i and j)**

Grayscale analysis of western blot in HUC-MSC. Statistical results of the expression of total Nrf2, HO-1, GSS and Trx compared with internal reference protein GAPDH. Experiments were repeated 3 times. Data were presented as mean ± SD, P values were calculated using T-test. ns, not significant; ****p< 0.0001.

Fig. S3 CAP increases ATP content and inhibits LA production.

(a) The content of ATP in GES-1 cells in different treatment groups. Data are presented as mean ± SD, P values were calculated using T-test. ns, not significant; **p< 0.01. # p< 0.0001 (EtOH compared with the Ctrl). **(b)** CAP (8 μM) pretreatment for 2.5 h and 5% EtOH incubation for 1.5 h, the intracellular LA level was measured. Data were presented as mean ± SD, P values were calculated using T-test. # p< 0.0001(EtOH compared with the Ctrl); **p< 0.01. ***p< 0.001 (CAP + EtOH compared with the EtOH). **(c)** Schematic diagram of intracellular glycolysis. **(d and e)** Detection of the mRNA level of *PKM2* and *LDHA* in different treatment groups. Data were presented as mean ± SD, P values were calculated using T-test. ns, not significant; *p< 0.05; **p< 0.01.

Fig. S4 Capsaicin protects 293T from oxidative stress.

(a) Expression of KEAP1 in human KEAP1 knockout 293T cells (293T KO). **(b and c)** The grey analysis of NRF2 and HO-1 of each group in 293T. Data were presented as mean ± SD, P values were calculated using T-test. ****p< 0.001. **(d and e)** The grey analysis of NRF2 and HO-1 of each group in 293T(KO). Data were presented as mean ± SD, P values were calculated using T-test. ****p< 0.001.

Fig. S5 Molecular dynamics simulations of CAP and Kelch.

(a) The binding energy landscapes of the molecular docking of CAP and KEAP1. **(b)** NRF2 associated with Keap1 in the absence of CAP. Majority of frames throughout the 100 ns trajectory featured NRF2 binding with Keap1. **(c)** The distribution of NRF2 fragments around Keap1 (gray color) in the presence

of CAP (represented as yellow ball/stick). The representative conformations of NRF2 throughout the simulations were superimposed on KEAP1. **(d)** The averaged distance between NRF2 Asp29 and Keap1 Arg415 (represented as green sticks) were measured and recorded in the MD simulations. **(e)** The distance between NRF2 Asp29 and KEAP1 Arg415 in the NRF2-KEAP1 complex (black line) and the NRF2-CAP-KEAP1 complex (red line).

Fig. S6 MS/MS and Co-IP analysis of CAP and Kelch.

(a) MS/MS of KEAP1 peptide containing Cys257 after CAP treatment. **(b)** MS/MS of KEAP1 peptide containing Cys273 and Cys288 after CAP treatment. **(c)** MS/MS of KEAP1 peptide containing Cys434 after CAP treatment. **(d)** MS/MS of KEAP1 peptide containing Cys613 after CAP treatment. **(e)** The grey analysis of NRF2 in IP group and in the supernatant of each group. Data were presented as mean ± SD, P values were calculated using T-test. ns, not significant; *p< 0.05; ***p< 0.001; ****p< 0.001.

Fig. S7 Biosafety and concentration determination of IR-HSA@CAP.

(a and b) IR-HSA@CAP NPs including HSA (0.04 mg/ml) and CAP (0.02 mg/ml) were added into GES-1 and Raw264.7 cells for 24 h to assess biosafety. **(c)** Standard curve for determination of CAP by HPLC. **(d)** The concentration of CAP released from IR-HSA@CAP NPs (including 0.4 mg/ml CAP) after a certain period of treatment in SGF by HPLC. **(e)** The concentration of CAP released from IR-HSP@CAP NPs (including 0.4 mg/ml CAP) was measured in SGF and SPSS for 30 min respectively.

Fig. S8 Safety evaluation of animal experiments.

(a) A model diagram of safety trial about CAP and IR-HSA@CAP NPs in rats. **(b and c)** Organ index of liver and spleen. ns, not significant. Data were presented as mean ± SD, P values were calculated using T-test. ns, not significant. **(d-f)** Determination of ALT, AST and T-Bil in serum to evaluate liver

function. **(g-i)** Determination of BUN, CRE and UA in serum to evaluate renal function. Data were presented as mean ± SD, P values were calculated using T-test. ns, not significant. **(j-m)** Western blot analysis of antioxidant protein expression of NRF2, HO-1 and Trx. Data were presented as mean ± SD, P values were calculated using T-test. ns, not significant; *p< 0.05; ***p< 0.001; ****p< 0.001.

Supplementary Video S1: Molecular dynamics simulations between NRF2 and Kelch. **Supplementary Video S2:** Molecular dynamics simulations between NRF2 and Kelch in the presence of CAP.

SUPPLYMENTART FIGURES

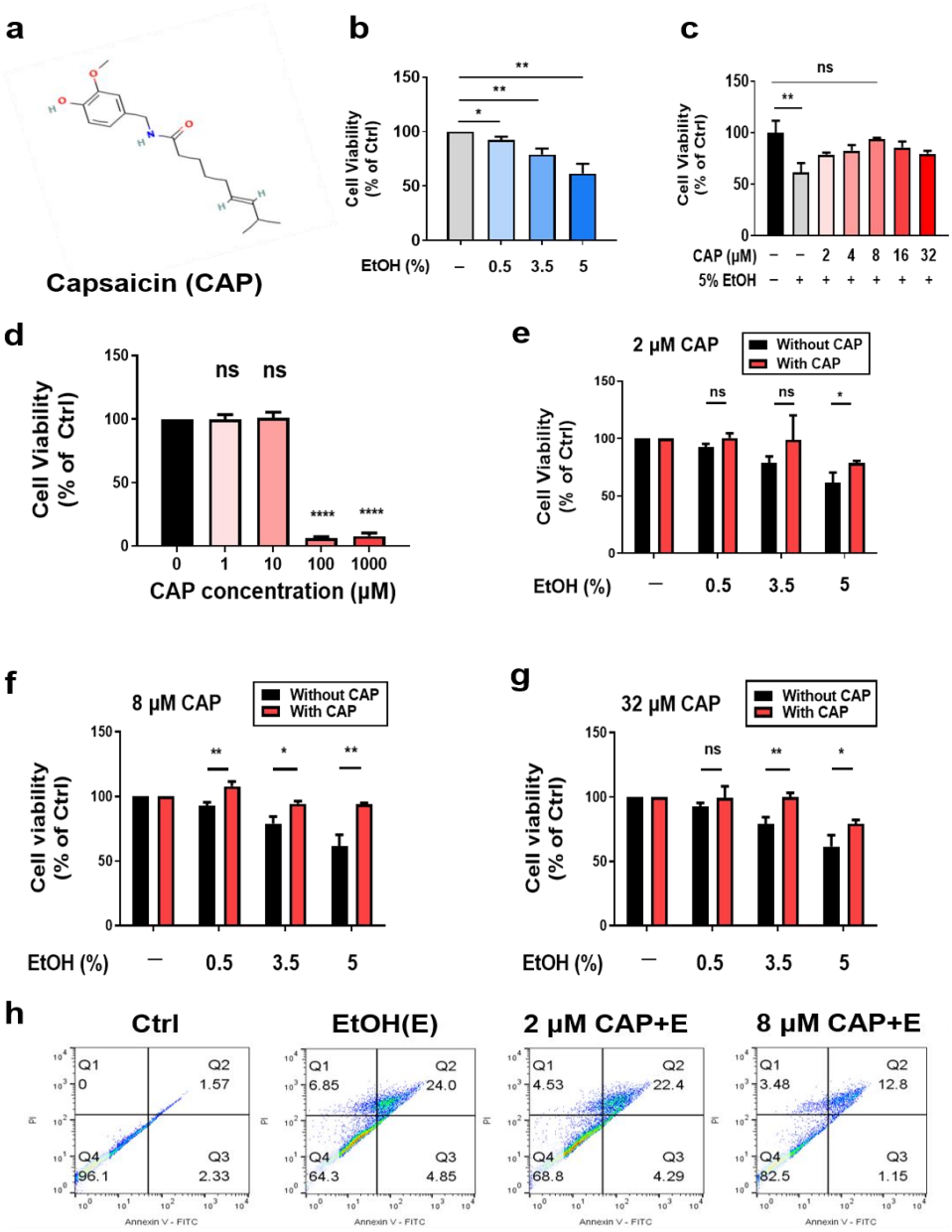

Supplementary Figure 1

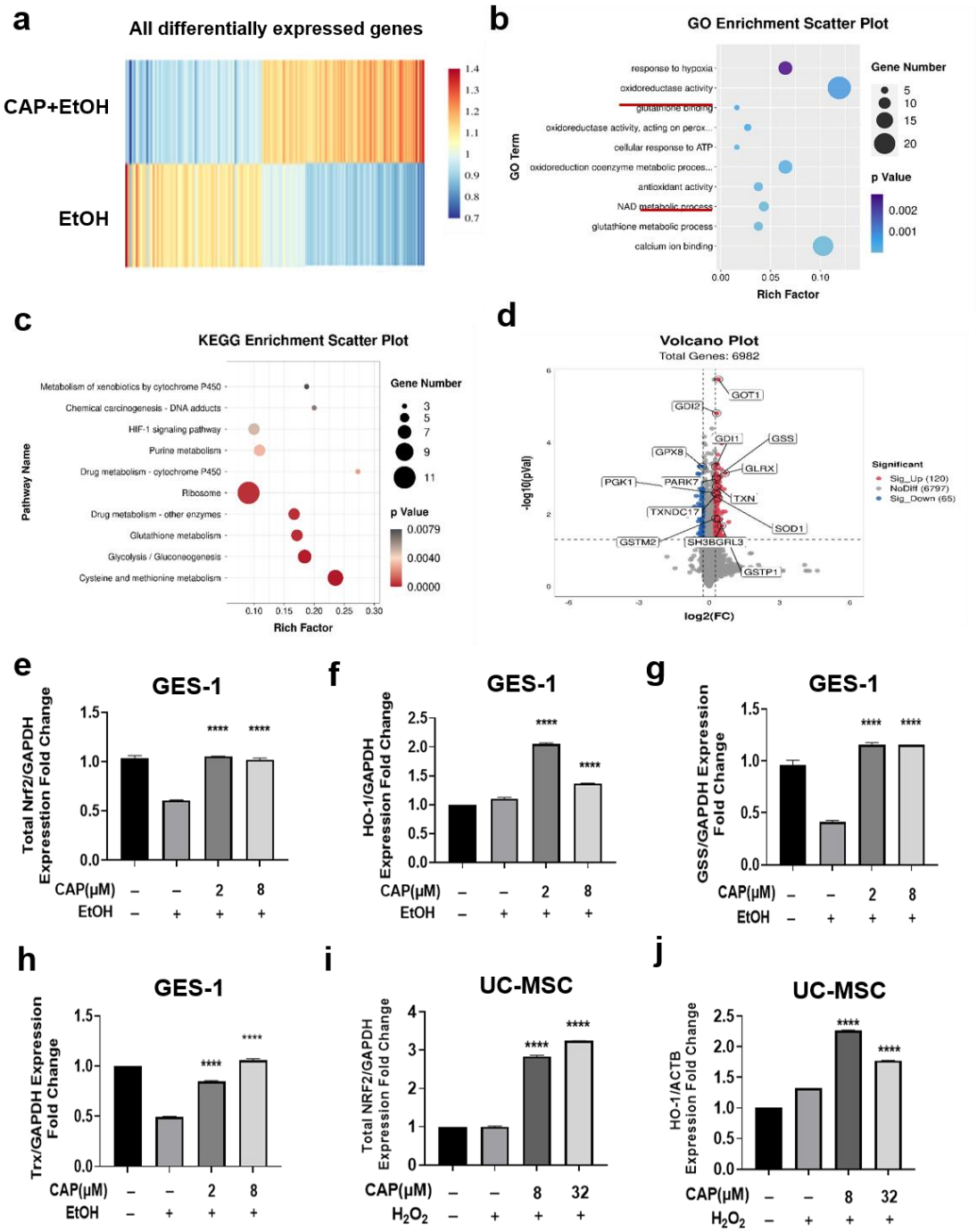

Supplementary Figure 2

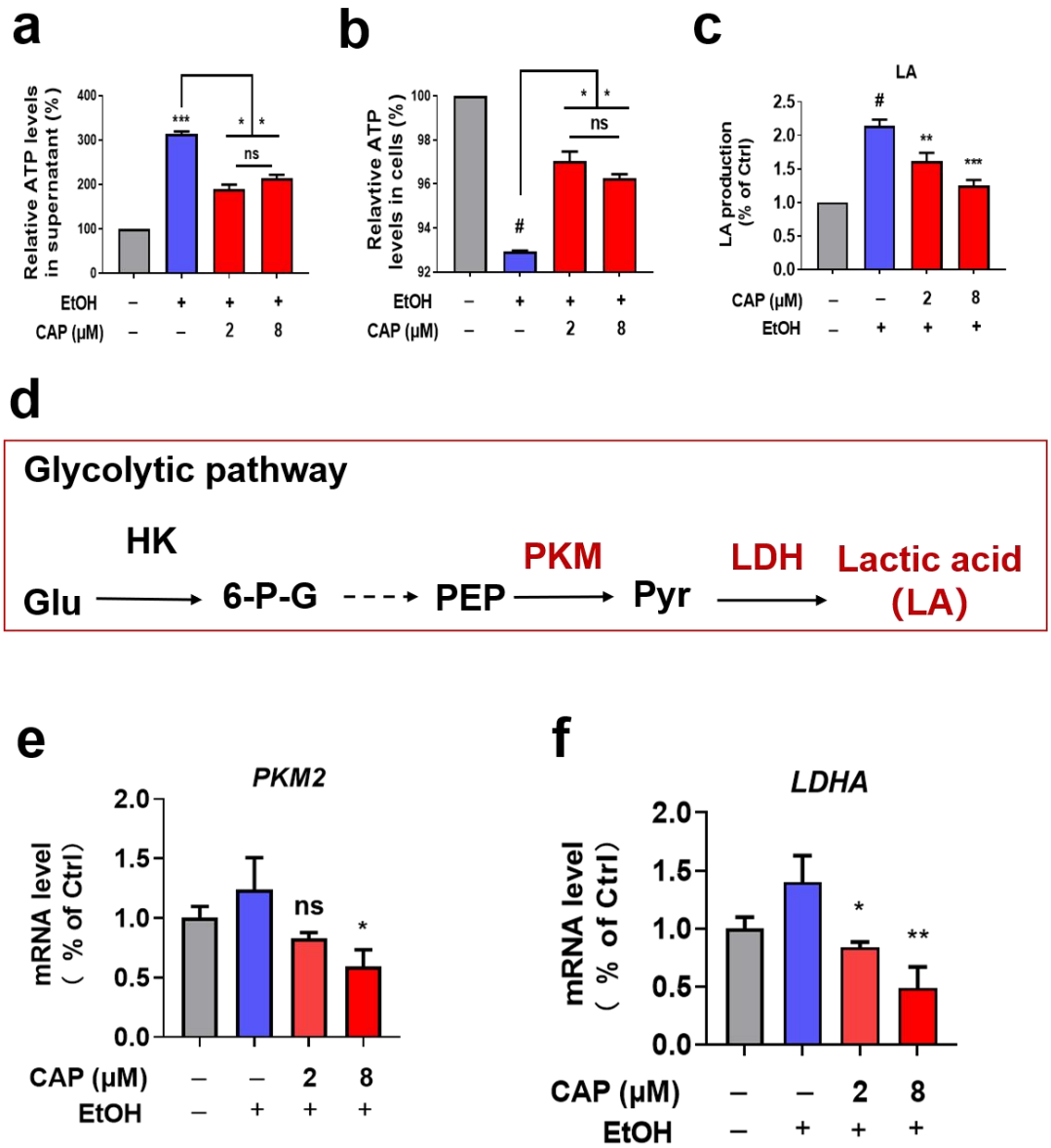

Supplementary Figure 3

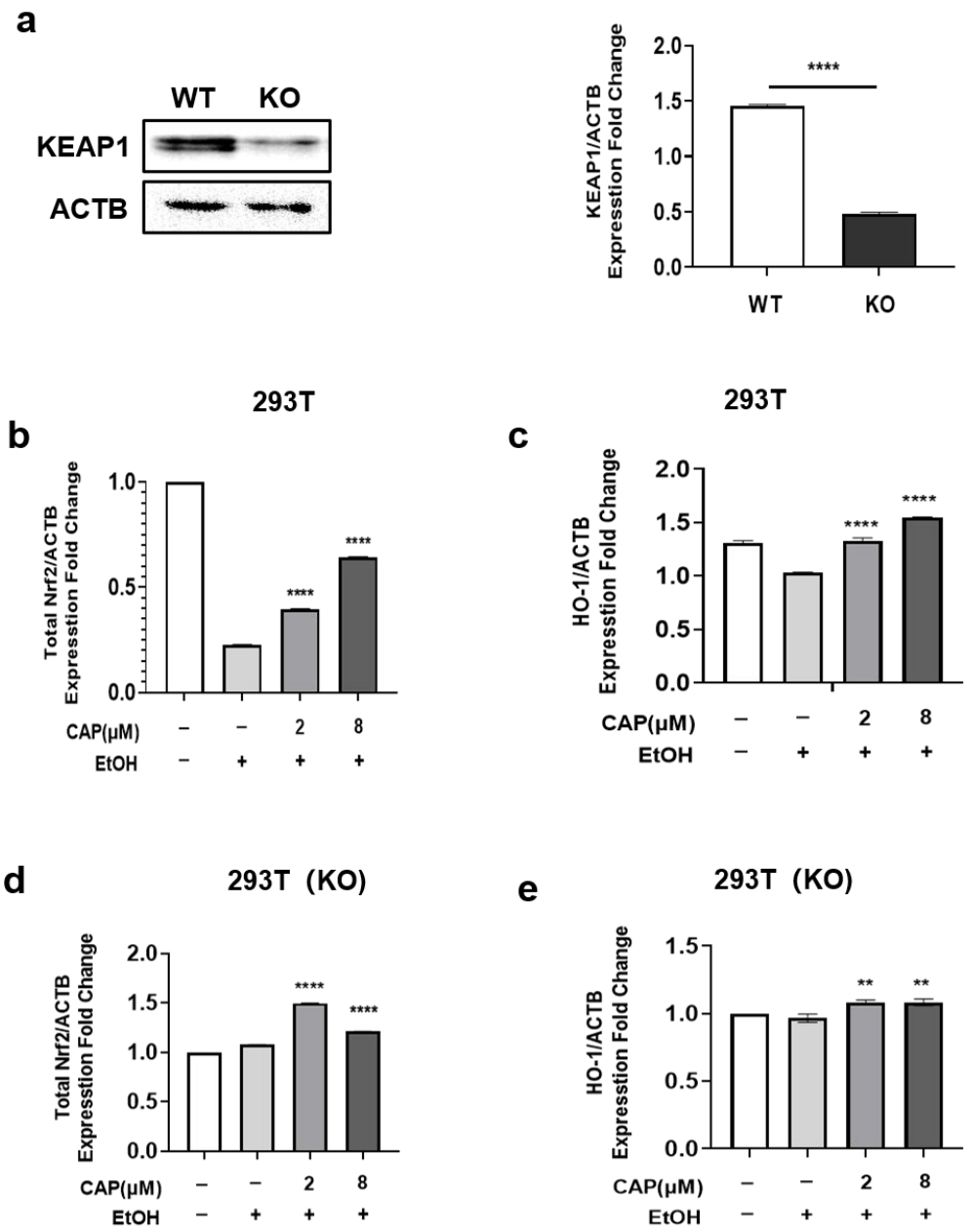

Supplementary Figure 4

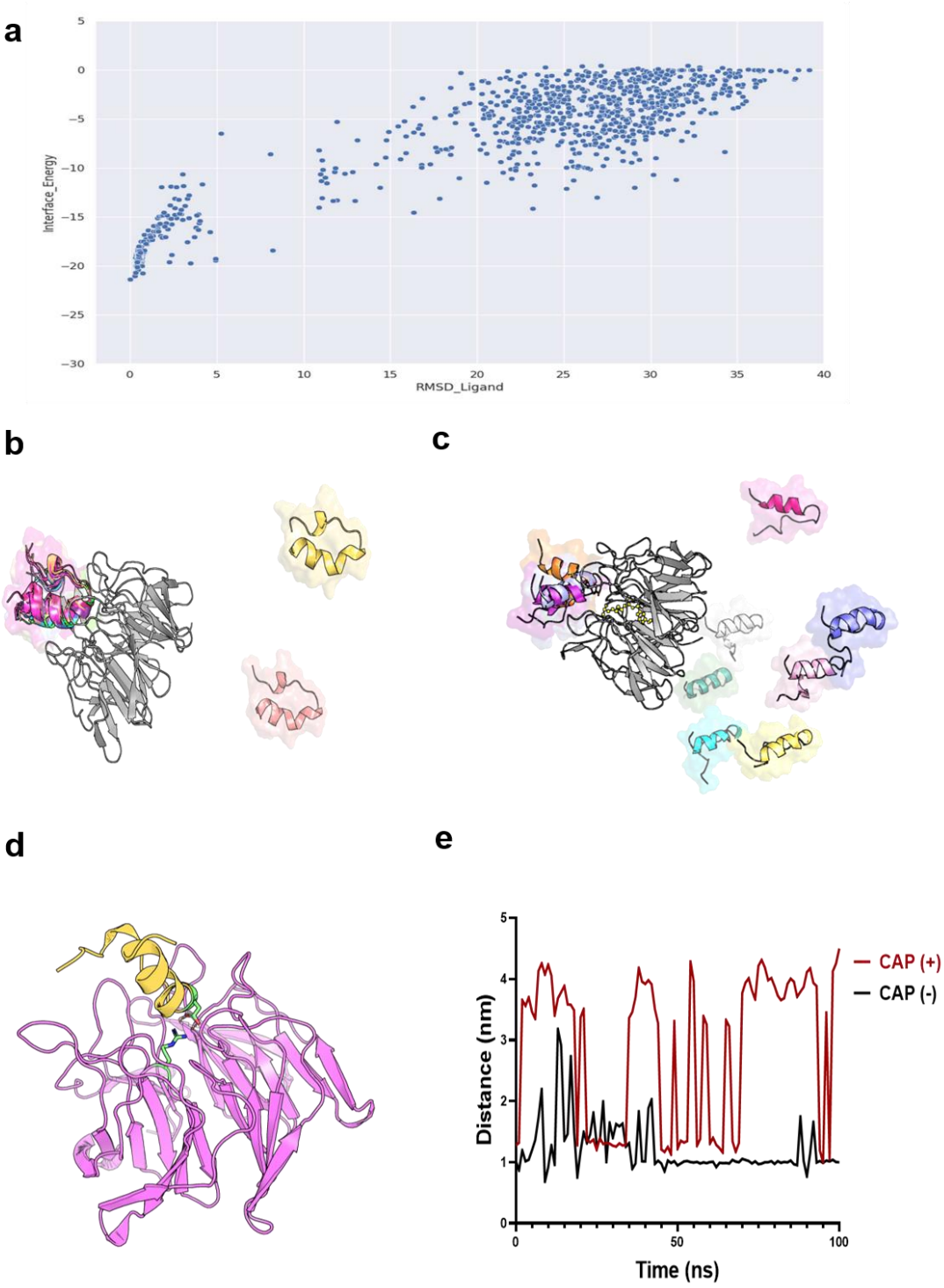

Supplementary Figure 5

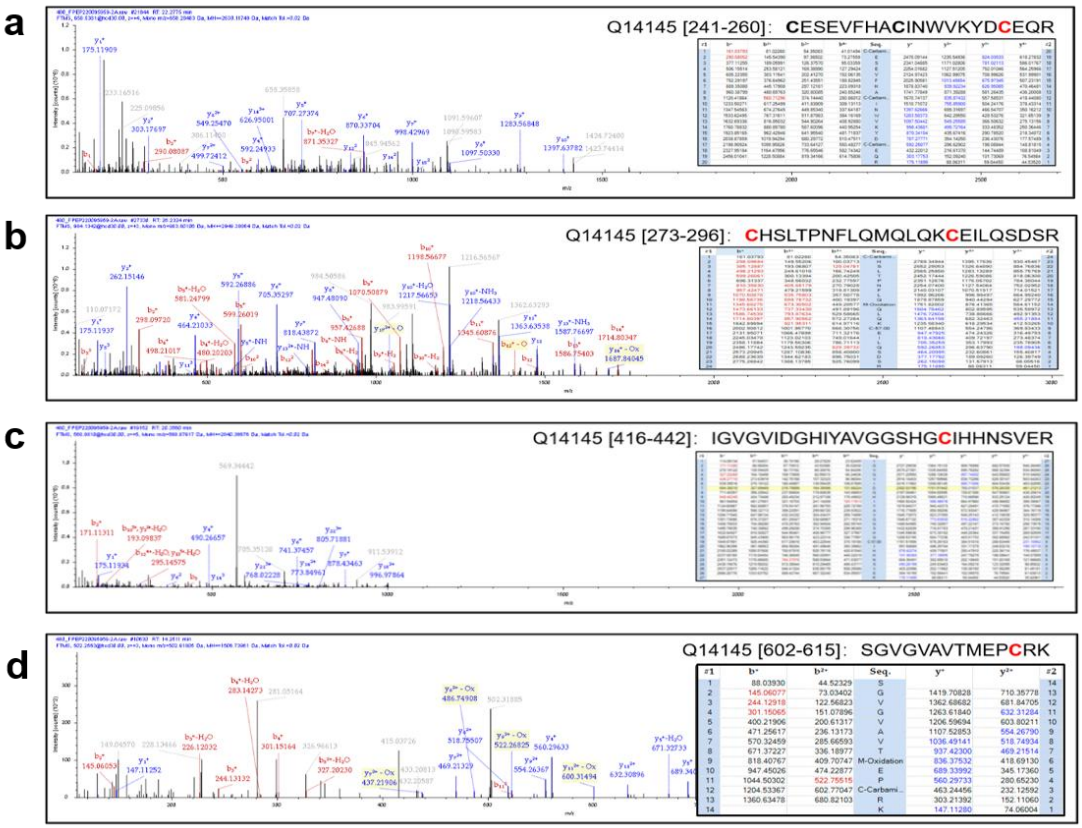

Supplementary Figure 6

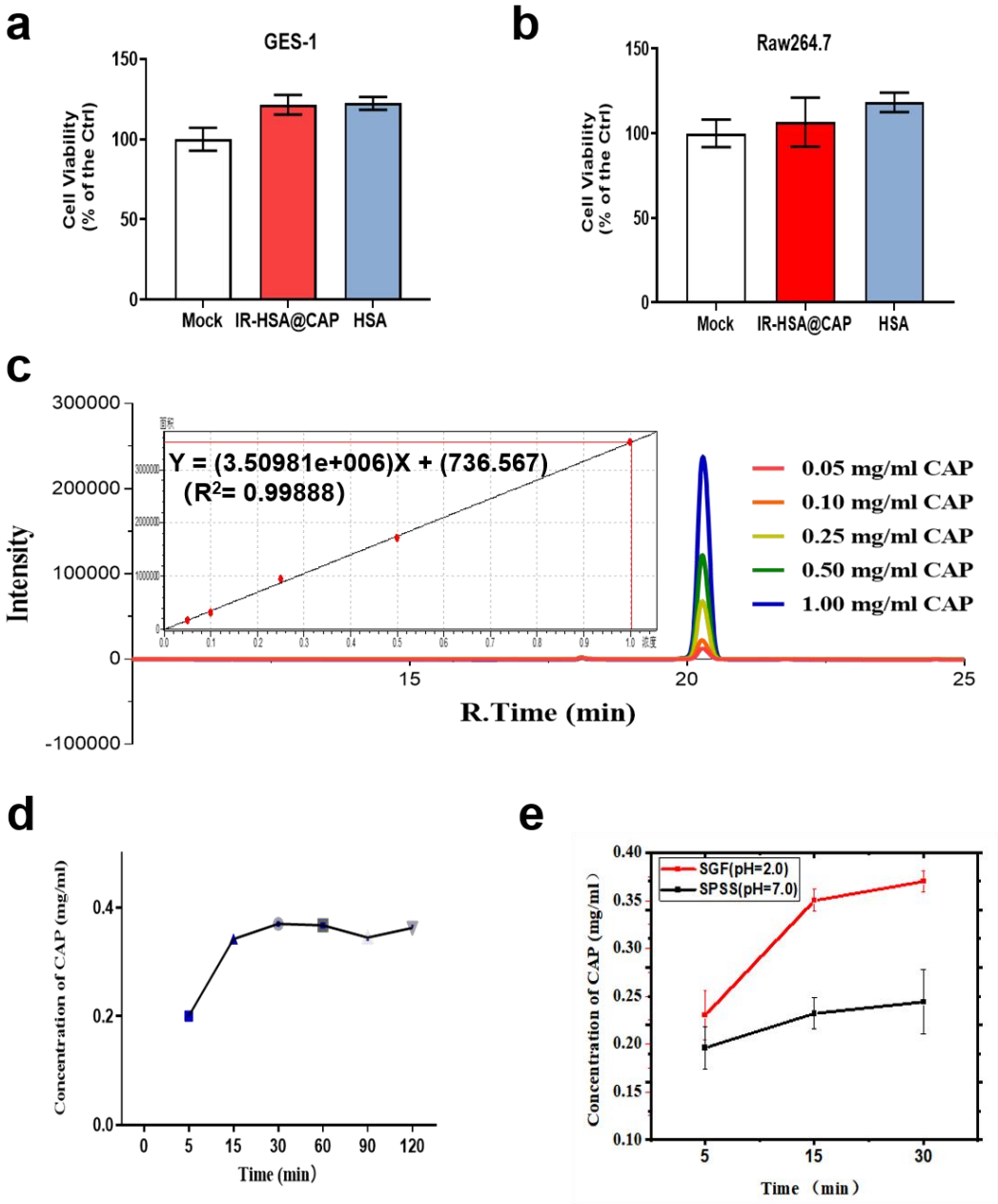

Supplementary Figure 7

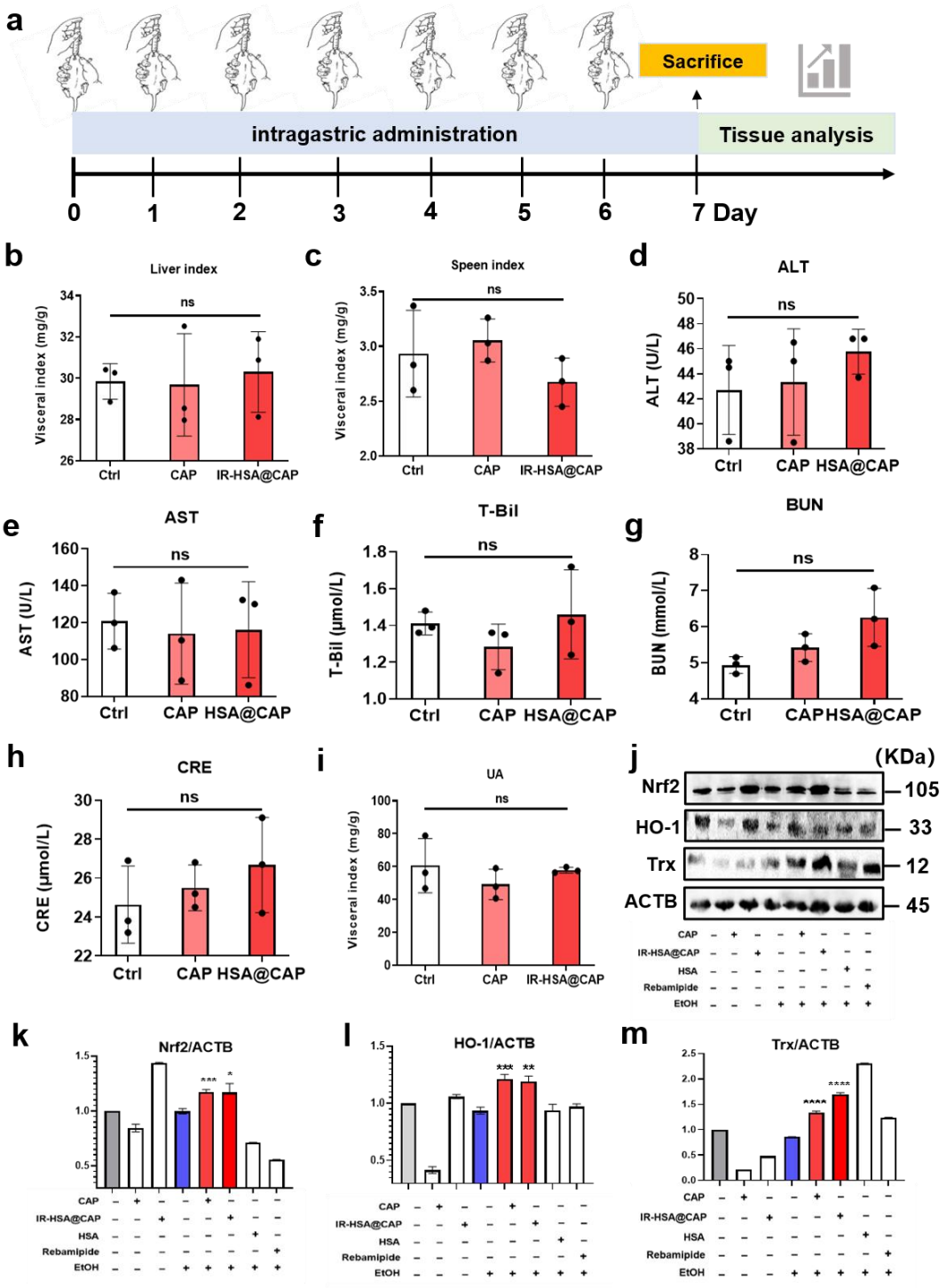

Supplementary Figure 8